# Ground deformations and volcanic processes as imaged by CGPS data at Mt. Etna (Italy) between 2003 and 2008

Valentina Bruno,[1] Mario Mattia,[1] Marco Aloisi,[1] Mimmo Palano,[1] Flavio Cannavò,[1] and William E. Holt[2]

Received 20 December 2011; revised 22 May 2012; accepted 1 June 2012; published 21 July 2012.

[1] We analyze the kinematic and crustal deformations of Mt. Etna from 2003 to 2008 as imaged by the Mt. Etna continuous GPS (CGPS) network (Etn@net). Through a careful analysis of GPS time series, six coherent phases of crustal deformations have been identified, three inflation phases and three deflation phases, superimposed on a major inflation of the volcanic edifice since 2001. The inversions of GPS velocities have enabled: 1) a better understanding of the evolution of the volcanic sources acting beneath the volcano; 2) analysis of the strain rate patterns; and 3) a delineation of potential coupling between volcanic sources and the observed ground deformations. The modeling of the pressure sources has shown a separation between inflation and deflation sources. The deflation sources show an upward migration, from 5.5 toward 2.0 km (b.s.l.), while the inflation sources are located within 5.5 and 4.0 km (b.s.l.). Our results indicate that the kinematic and ground deformations of the mid-upper eastern flank are driven by the interplay between the effect of the magmatic sources and a southeastward motion. Furthermore, clockwise rotations have been detected that prevailed over the eastern motion of the flank during the inflation phases preceding the 2004–2005 and 2006 eruptions. Finally, the accordance between the higher geodetic shear strain rates and the area with the highest seismic energy release shows that measured geodetic shear strain rates can provide useful information on the potential occurrence of seismic activity.

**Citation:** Bruno, V., M. Mattia, M. Aloisi, M. Palano, F. Cannavò, and W. E. Holt (2012), Ground deformations and volcanic processes as imaged by CGPS data at Mt. Etna (Italy) between 2003 and 2008, *J. Geophys. Res.*, *117*, B07208, doi:10.1029/2011JB009114.

## 1. Introduction

[2] Knowledge of the GPS velocity field of active volcanoes is important for several reasons. It allows us to infer information about the physics of the underlying deformation and to investigate the shallow level magma migration, which is an essential tool for forecasting future eruptions. Furthermore, it enables monitoring ground deformations and deriving strain rate fields that are a potential input in earthquake hazard assessment.

[3] Velocity or displacement measurements began on Mt. Etna in 1988, when a network of GPS benchmarks was surveyed [*Puglisi et al.*, 2004]. Since then, this geodetic network has been surveyed by GPS almost yearly [*Palano et al.*, 2008]. In November 2000, a continuous GPS (CGPS) monitoring started. The permanent Mt. Etna GPS network (Etn@net) has been further improved, reaching the current configuration of 36 stations that almost entirely cover the volcanic edifice.

[4] In this paper we present, for the first time, the CGPS data recorded by the Etn@net network from February 2003 to August 2008. We perform an analysis of the CGPS time series in order to discuss the possibility of investigating time spans characterized by coherent crustal deformation patterns and in which homogeneous volcanic sources can clearly be distinguished. This is a crucial issue in volcanic areas such as Mt. Etna, characterized by large and fast deformations. In our view, geodetic techniques like episodic GPS or EDM campaigns or InSAR data, constrained by the time span between two successive data acquisitions, may be ill-suited to consider non-coherent deformation phases (e.g., characterized by inflation and deflation together) and consequently to model non-homogeneous volcanic sources and processes.

[5] After a close investigation of the time series, we provide an image of the sources related to deflation-inflation cycles, calculated through the analytical modeling of the recorded CGPS data. The aim of this kind of analysis is to improve knowledge of the processes related to magma migration beneath Mt. Etna and their temporal evolution.

[1]Osservatorio Etneo, Istituto Nazionale di Geofisica e Vulcanologia, Catania, Italy.
[2]Department of Geosciences, State University of New York at Stony Brook, Stony Brook, New York, USA.

Corresponding author: M. Mattia, Osservatorio Etneo, Istituto Nazionale di Geofisica e Vulcanologia, Piazza Roma 2, Catania IT-95123, Italy. (mattia@ct.ingv.it)


0148-0227/12/2011JB009114

Every single phase has been constrained in time and space and a possible logical framework connecting all the phases is proposed.

[6] We have also explored the potential of strain rate maps when applied to volcano monitoring. Their importance lies in synthesizing, in a simplified way, the large amount of information derived from a GPS velocity map. The mapped strain rate parameters can help us: 1) analyze the detailed features of the deformation pattern of the different portions of the volcano; 2) pick out rotation components in some areas; and 3) deduce where seismic activity might occur.

[7] The final step of this study is a comparison between the observed strain field, as described from the inversion of GPS velocities, and synthetic strain rate fields, as calculated starting from theoretical velocity maps obtained from the modeled active sources. The difference between the two strain maps has enabled identification of the magnitude and spatial extent of ground deformations due to non-volcanic processes (e.g., movements of local faults, creep phenomena, etc.).

## 2. Mt. Etna: Geological Setting

[8] Mt. Etna (Figure 1) is a Quaternary composite volcano, characterized by Na-alkaline magmatism, which has grown to its present elevation of about 3320 m by the accumulation of lavas and pyroclastics erupted during the last 200 kyr [*Gillot et al.*, 1994]. It is located at the front of the Maghrebian thrust belt on the footwall of a Late Quaternary east-facing crustal scale normal fault system [*Ellis and King*, 1991; *Monaco et al.*, 1997; *Hirn et al.*, 1997; *Bianca et al.*, 1999; *Nicolich et al.*, 2000; *Argnani and Bonazzi*, 2005], which has partially reactivated the Malta Escarpment, a Mesozoic discontinuity separating the continental crust of the Pelagian Block [Hyblean Plateau; *Burollet et al.*, 1978] from the oceanic crust of the Ionian Sea [*Makris et al.*, 1986]. The eastern and southern sectors of the volcano lie mostly on an Early Middle Pleistocene foredeep clayey succession, deposited on the flexured margin of the Pelagian block and containing several levels of basaltic pillow lavas and hyaloclastites dating back to 500–250 kyr [*Gillot et al.*, 1994].

[9] The tectonic setting of Mt. Etna is commonly interpreted as due to the interaction of regional tectonic and local-scale volcano-related processes. Recent focal mechanism analysis and stress tensor computations indicate that a dominant ca. N-S compressive domain in the lower crust (h > 10 km) beneath the western sector of Mt. Etna [e.g., *Patanè and Privitera*, 2001] coexists with a ca. ESE-WNW extensional regime [e.g., *Monaco et al.*, 2005]. Furthermore, the volcanic edifice is subject to local stress due to dike forming intrusions that ascend mostly along the North-East and South Rift zones. The most outstanding tectonic features at Mt. Etna are clearly recognizable on the eastern flank of the volcano, where morphological evidence of active faulting exists (Figure 1). In particular, the Pernicana fault system, on the northeastern flank, and the Mascalucia-Tremestieri-Trecastagni fault system, on the southeastern flank, are considered two of the most important features for understanding the dynamics of the volcano [*Lo Giudice et al.*, 1982]. According to many authors, these faults would be connected through the North-East Rift and South Rift, crossing the summit craters to define an unstable sector (Figure 1) [*Neri et al.*, 2004; *Rust et al.*, 2005]. This sector of the volcano is affected by a long-term sliding toward the ESE, resulting from the interaction between gravity, thermal effects, regional tectonics and dike intrusions [*McGuire and Pullen*, 1989; *Borgia et al.*, 1992; *McGuire et al.*, 1996; *Rasà et al.*, 1996; *Borgia et al.*, 2000; *Froger et al.*, 2001]. The eastern sector of the volcano is bordered to the east by two active NNW-SSE (the Acireale-Sant'Alfio system) and NNE-SSW (the Piedimonte system) faults systems called "Timpe," which can be considered the northernmost prolongation of the Malta Escarpment (Figure 1). These faults, roughly parallel, reach a length of about 10 Km, a vertical offset of more than 200 m and have been active since the Tortonian [*Monaco et al.*, 1995]. Conversely, in the western sector of Etna, there is only slight morphological evidence of faulting, such as some short segments of faults observable on the southwestern flank [*Monaco et al.*, 2010]. However, it should be considered that the faults with morphological evidence may represent only a part of the tectonic structures present in the Etnean area and hidden fault segments could be covered by the huge pile of volcanic products [e.g., *Azzaro*, 1999]. Indeed, most recent seismic studies [*Bonaccorso and Patanè*, 2001; *Bonaccorso et al.*, 2004; *Patanè et al.*, 2005] show the existence of several notable segments of unknown faults, ca. NE-SW and ENE-WSW oriented, both on the western [6–8 km length, *Bonaccorso et al.*, 2004; *Bonanno et al.*, 2011] and on the east-northeastern [up to 10 km length, *Patanè et al.*, 2005] flanks of the volcano.

## 3. Volcanological Patterns During the Period 2003–2008

[10] Our analysis starts from the end of the deflationary phase related to the 2002–2003 eruption. This eruption was characterized by the opening of two distinct fractures along the upper northeastern and southern flank and was preceded by very few precursors in terms of seismicity and ground deformation [*Monaco et al.*, 2005; *Aloisi et al.*, 2003]. Such a highly explosive eruption had not been observed at Mt. Etna since the 1783 event. Another peculiar feature of this eruption was the contemporary emission of two compositionally distinct magmas from the two different fractures [*Andronico et al.*, 2005; *Ferlito et al.*, 2009, 2012]. The eruption ended on 28 January 2003 and the total amount of lava emitted has been estimated at $\sim$33–46 $\cdot$ $10^6$ $m^3$ [*Andronico et al.*, 2005].

[11] Following the 2002–2003 eruption, Mt. Etna remained quiet for more than 19 months. During this period, some of the summit vents showed continuous degassing with occasional flurries of deep-seated explosive activity [*Allard et al.*, 2006]. On 7 September 2004, a new flank eruption began on the eastern flank, along a system of E-W and NNE-SSW oriented fractures (Figure 1). The 2004–2005 eruption was entirely different from the 2002–2003 one and was characterized by an outpouring of degassed magma. The peculiar characteristic of this eruption was the absence of any geophysical and geochemical precursor and its slow initial evolution [*Burton et al.*, 2005]. Following the hypothesis of some authors [*Burton et al.*, 2005], this eruption was triggered by the coupling between the strain related to the accumulated stress in the unstable eastern sector of the volcano and the recharge process (inflation) that followed the 2002–2003 eruption, allowing the degassed magma residing

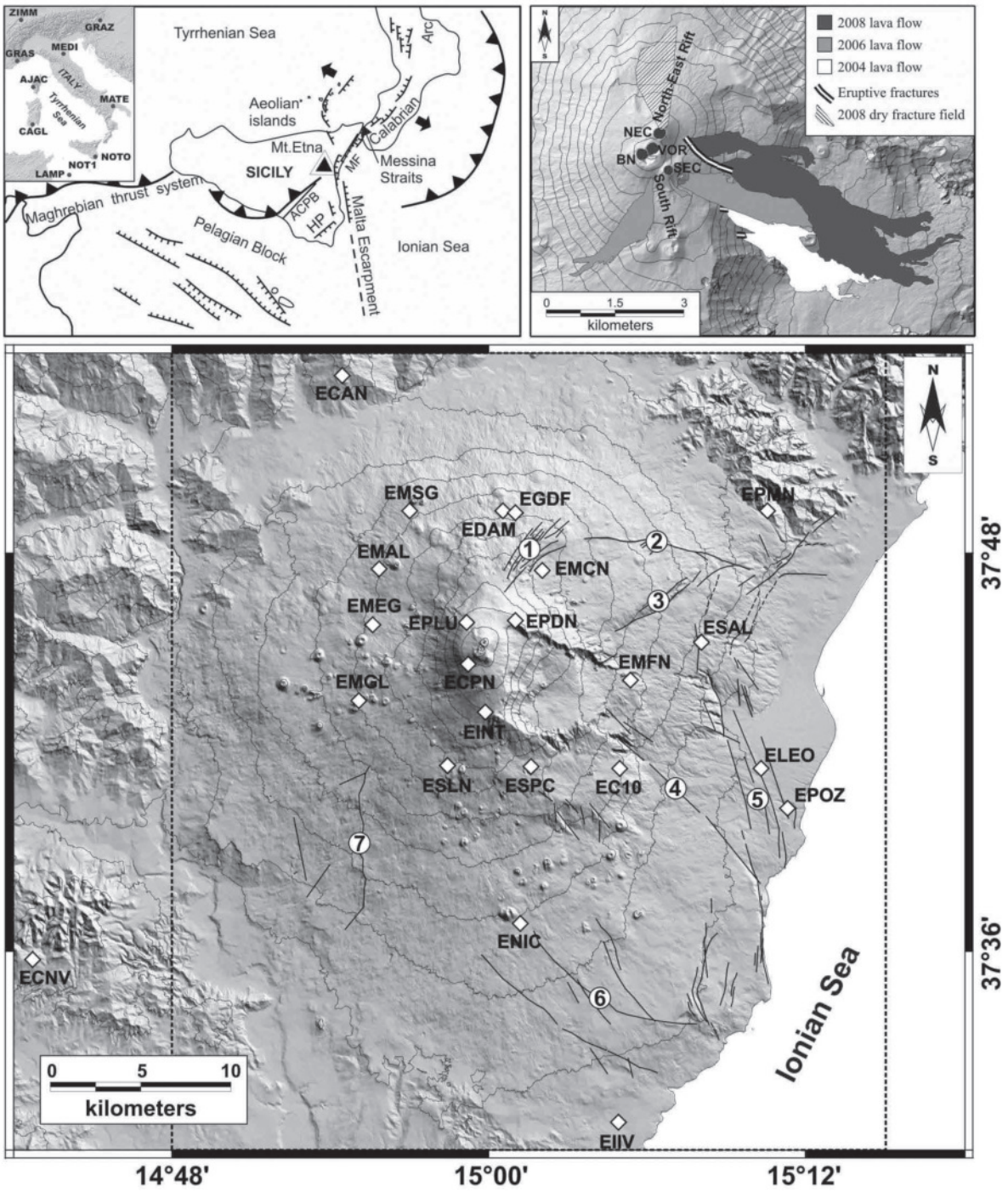


**Figure 1.** (bottom) Sketch map of Mt. Etna: (1) North-East Rift; (2) Pernicana fault; (3) Ripe della Naca fault; (4) Santa Venerina fault; (5) Timpe fault system and Moscarello fault; (6) Mascalucia-Tremestieri-Trecastagni faults system; (7) Ragalna fault. Mt. Etna Permanent GPS network (Etn@net termed) is also reported (white diamonds). Dotted box delimits the area reported in Figures 6–11. (top left) The location of Mt. Etna in the central Mediterranean area: MF, Messina-Fiumefreddo line; HP, Hyblean Plateau; ACPB, Acate-Caltagirone-Ponte Barca line. The location of IGS CGPS stations introduced into the processing (black points) is also shown. (top right) The summit craters: NEC, Northeast Crater; VOR, Voragine; BN, Bocca Nuova; SEC, Southeast Crater. Lava flows of the 2004–2005, 2006 and the 2008 eruptions are also reported, together with the eruptive fractures.

in the superficial plumbing system of the Southeast Crater (Figure 1) to pour out. The eruption ended in March 2005.

[12] On 14 July 2006, a new eruption started from a vent at the base of the Southeast Crater [*Neri et al.*, 2006b]. After the onset of the eruption the volcanic tremor slowly increased and a new vent opened three days later. A few days after, the maximum level of amplitude of the volcanic tremor was reached and some episodes of lava fountaining were observed. Like the 2004 eruption, this eruption was not accompanied by evident geophysical parameter changes, even if the 2006 eruption was characterized by strong degassing from the uppermost vent, with strong strombolian activity. The eruption ended on 23 July 2006. The volcanic activity restarted at the Southeast Crater at the end of August 2006, with strombolian activity and the formation of new short lava flows expanding eastward for about 1 km [*Bonforte et al.*, 2008]; the activity lasted until mid-September. A new eruptive fracture opened on 13 October from the eastern base of the Southeast Crater, along an ESE-WNW trend, and an effusive activity started forming lava flows that spread eastward. On 26 October, a new fracture opened on the opposite side of the Southeast Crater, involving also the southern flank of the Bocca Nuova Crater. The opening of the fractures was not accompanied by geophysical parameter changes. Only episodic increases in volcanic tremor accompanied the more intense degassing events and the strombolian activity [*Bonforte et al.*, 2008]. The eruption activity ended on 15 December 2006 [*Bonforte et al.*, 2008].

[13] Between 2006 and 2008, many episodes of explosive activity and lava fountaining were observed at the summit area of the volcano. In particular, the episodes of 4–5 September 2007, 23–24 November 2007 and 10 May 2008 were noteworthy [*Andronico et al.*, 2008].

[14] On 13 May 2008 a new eruption started from a dike which propagated from the summit area toward the NNW direction for about 2.5 km and with a width of about 800 m (Figure 1) [*Aloisi et al.*, 2009]. Unlike the 2004–2005 and 2006 eruptions, the initial phase of the May 2008 eruption was preceded and accompanied by strong seismic release. Indeed, more than 230 events located in the northeastern area were recorded on 13 May [*Aloisi et al.*, 2009]. Furthermore, the beginning of the eruption was accompanied by marked deformations, measured by permanent GPS and tilt networks, and lava fountaining activity [*Aloisi et al.*, 2009]. The eruptive event, characterized by an almost steady magma supply, lasted until July 2009.

## 4. Geodetic Network and Data Processing

[15] The continuous GPS (CGPS) monitoring of ground deformations on Mt. Etna started in November 2000. Since then the Etn@net permanent network has been improved, reaching the configuration of 13 stations already by 2003, up to the current configuration of 36 GPS stations that cover most areas of the volcano edifice (Figure 1). In this paper, data collected by the Etn@net network between the end of the 2002–2003 eruption and the beginning of the 2008 eruption have been analyzed in order to investigate the ground deformation pattern affecting the Mt. Etna volcano during this period.

[16] The CGPS data were processed with the GAMIT/GLOBK software [*King and Bock*, 2004; *Herring*, 2004] packages with IGS (International GNNS Service - http://igscb.jpl.nasa.gov) precise ephemerides and Earth orientation parameters from the International Earth Rotation Service (http://www.iers.org) Bulletin B.

[17] Data from 9 continuously operating IGS stations (AJAC, CAGL, GRAS, GRAZ, LAMP, MATE, MEDI, NOT1 and NOTO; Figure 1) were also included in the processing with the GAMIT software to combine the daily individual solutions in GLOBK with estimates obtained from a similar analysis at the Scripps Orbit and Permanent Array Center (ftp://garner.ucsd.edu/pub/hfiles) of observations from continuous GPS stations of the regional EURA network. By using the GLORG module of GLOBK [*Herring*, 2004] the loosely constrained daily solutions were transformed into the ITRF2005 reference frame [*Altamimi et al.*, 2007] and then rotated into the Etn@ref local reference frame [*Palano et al.*, 2010].

[18] Detailed studies of CGPS data indicate that the noise in GPS time series may be characterized by a combination of random (white) and correlated (colored) noise that depends on several factors, i.e., satellite and tracking network, monument stability, atmospheric conditions, etc. [*Mao et al.*, 1999; *Dixon et al.*, 2000]. In GPS processing with GLOBK, noise is usually added as a time dependent random walk error in the velocity estimation. Following the procedure described in *McCaffrey et al.* [2007], we added 1 mm/yr$^{1/2}$ and 2 mm/yr$^{1/2}$ of random walk noise in the horizontal and vertical coordinates respectively in our processing, which represent appropriate values for Mt. Etna CGPS data.

[19] The results of the processing are reported here in terms of GPS velocity fields and time series of the length variations between GPS stations.

## 5. Ground Deformation Pattern From CGPS Data

[20] In order to detect the different volcanic phases of Mt. Etna, we have analyzed the time series of the length variations between the EMAL and EMGL stations (Figure 2). The capacity to track inflation-deflation phases through GPS baselines length variations has already been highlighted in *Aiuppa et al.* [2010] and in *Patanè et al.* [2005]. Here we use the EMAL-EMGL baseline measured from 2003 to 2008, to precisely constrain the timing of the changes in the deformation style at Mt. Etna. We have selected the EMAL-EMGL baseline among all the possible choices because: 1) both stations are located on the western flank of the volcano (Figure 1) that, as postulated by some authors, shows a nearly elastic response to the inflation/deflation phases [*Bonaccorso and Davis*, 2004; *Patanè et al.*, 2005]; 2) the GPS stations are continuously operating throughout the investigated time period; 3) the length variations between EMAL and EMGL stations is closely linked to the eruptive cycle as they are outside any standard noise sources that are usually considered to affect CGPS time series [*Mao et al.*, 1999].

[21] If we assume that any change in the deformation style of a volcano means that the source of the deformation itself is changing (in position, volume or both), the obvious consequence is that the constraint of timing, coupled with a

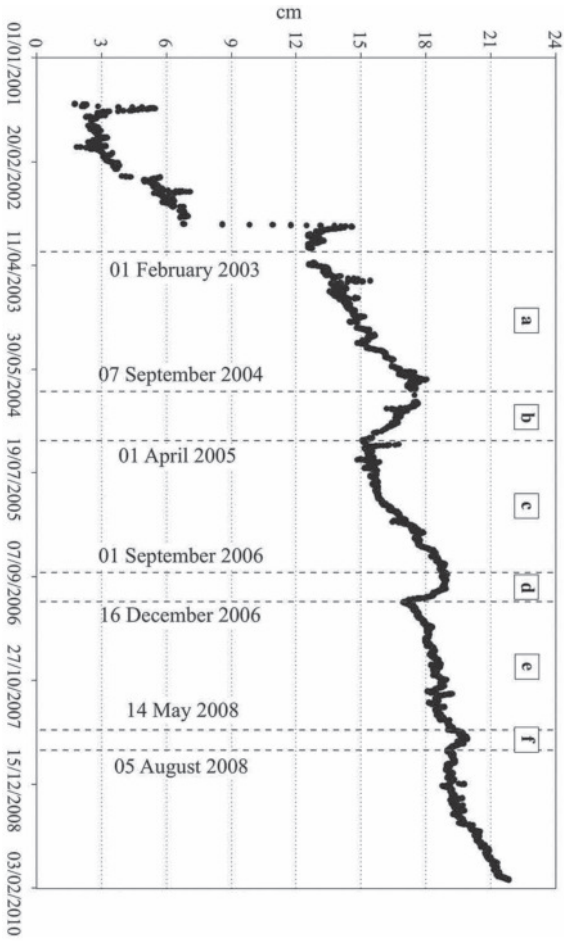


**Figure 2.** Time series of the length variations between the EMAL and EMGL CGPS stations. Vertical dotted lines separate the six different periods of volcanic activity, recognized on the basis of the changes in the slope of the baseline: February 01, 2003–September 06, 2004 (period a); September 07, 2004–March 31, 2005 (period b); April 01, 2005–August 31, 2006 (period c); September 01, 2006–December 15, 2006 (period d); December 16, 2006–May 13, 2008 (period e); May 14, 2008–August 4, 2008 (period f).

good spatial coverage of GPS stations over the volcanic area, is fundamental for a correct estimation of the ground deformations sources. Moreover, as testified by Figure 2, Mt Etna is subject to large and fast deformations and the risk of confusing the contribution of different volcanic sources is high when applying "non-continuous" geodetic investigations (periodical field campaigns or InSAR data).

[22] By analyzing Figure 2, we can observe that the baseline length increases during volumetric changes of magma (or probably during the upraise of a batch of magma) that induces the edifice to grow, and decreases during and after the eruptions, when magma outpours. Accordingly, we can identify six different periods of volcanic activity, three inflation phases forerunning respectively the 2004–2005, 2006 and the 2008 eruptions, and three deflation phases occurring during these three eruptions. More specifically the investigated time intervals are: a) February 01, 2003–September 06, 2004; b) September 07, 2004–March 31, 2005; c) April 01, 2005–August 31, 2006; d) September 01, 2006–December 15, 2006; e) December 16, 2006–May 13, 2008; f) May 14, 2008-August 4, 2008. The timing of the short-time variations identified in the EMAL-EMGL baseline shows a good correspondence with the observed volcanic activity.

[23] Furthermore, we have noticed that the short-term variations (from ~3 months to ~1.5 years) in the time series of the EMAL-EMGL baseline overlie a major inflation of the volcanic edifice, that corresponds to a roughly linear increase of the EMAL-EMGL relative distance since 2001 (Figure 2).

[24] Indeed, the length of the EMAL-EMGL baseline increased by about 10 cm from 2003 till the end of 2009. The lengthening of the baseline reaches a value of about 20 cm if we consider the variation since July 2001, including also the considerable offset (of about 7 cm) recorded between October and November 2002 (2002–2003 eruption). This pattern indicates that the volcanic edifice was inflating at least since 2003 and that this main process is accompanied by minor short-time inflation/deflation phases.

[25] For each different volcanic phase that has been identified through the analysis of the time series of the EMAL-EMGL baseline, we have computed the velocities of GPS stations in the local Etn@ref reference frame [*Palano et al.*, 2010], by approximating the observed deformation through linear velocities. Figure 3 shows that the Etnean velocity fields are characterized by a well-defined and marked radial pattern on the upper eastern, western, southern and northern flanks of the volcano. Differences with respect to a radial pattern were observed on the lower eastern flank of Mt. Etna where the CGPS stations move toward South-East throughout the analyzed time period.

[26] In particular, the CGPS stations move radially outward during recharging phases or intrusion processes, while an inward motion is observable during the deflations of the volcanic edifice that accompany eruptive events. In these two different situations, the magnitudes of the horizontal velocities are quite different. We can observe that during deflation episodes (Figures 3b, 3d, and 3f) the CGPS stations in the summit areas and along the western flank of the volcano move with velocities that are in general at least twice as great as those measured for the same stations during inflations (Figures 3a, 3c, and 3e), in agreement with the rapid change of the slope of the EMAL-EMGL baseline (Figure 2) observed during the deflation phases. On the contrary, the magnitude of the horizontal velocities is in general greater during inflation periods along the low and mid-upper eastern flank of the volcano compared these same stations during deflation.

[27] The behavior of the mid-upper eastern flank stations suggests that the GPS velocities can be considered as the result of two different components having a similar direction: 1) a radial component (inward or outward directed) due to volcanic processes (inflation/deflation phases) and 2) a southeastern component due to the anomalous displacements of the eastern flank. In particular, during the inflation phases the two components have the same orientation (both along a southeastern direction) and their effects combine, while during the contractions of the volcanic edifice, the southeastern directed

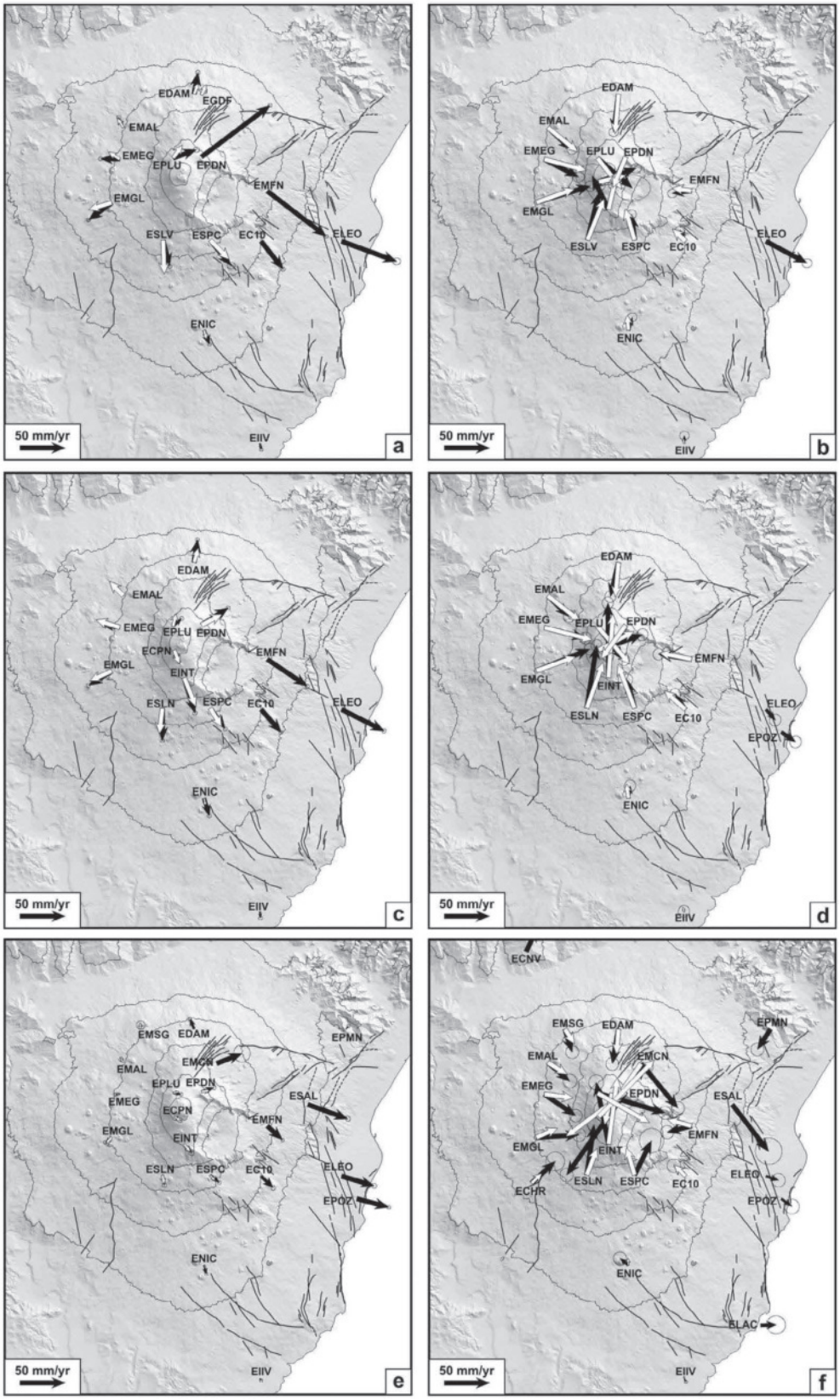


**Figure 3.** Observed horizontal GPS velocities (black arrows) with 95% confidence ellipses in the Etn@ref reference frame [*Palano et al.*, 2010] and modeled (white arrows) horizontal velocity field for each phase obtained using the *Yang et al.* [1988] model.

velocities are maintained only by the stations of the lower eastern flank. In this last case, the radial inward directed component prevails over the component due to the south-eastern motion of the eastern flank, inducing a lower module of the velocities of the mid-upper eastern flank stations with respect to the stations of the rest of the volcanic edifice.

[28] Figures 3a and 3c show that the velocity fields characterizing the inflation phases preceding the 2004–2005 and 2006 eruptions are comparable. The most evident differences concern the stations EPLU and EPDN, in the summit craters area, which underwent a decrease in their horizontal velocities, from 27.5 mm/yr and 95.0 mm/yr respectively before the 2004–2005 eruption, to 12.6 mm/yr and 35.5 mm/yr during the new inflation phase that followed that eruption, and EMFN, located on the eastern flank, that changed its velocity from 82.3 mm/yr to 56.3 mm/yr. Also, stations EC10 and ELEO of the eastern flank show a decrease in their velocities by about 6 mm/yr and 12 mm/yr, respectively (Figures 3a and 3c). Nevertheless, while the stations EMFN and EC10 change their motion from the southeast direction to a centripetal pattern toward the summit craters, during the 2004–2005 and 2006 eruptive events, the station ELEO continues moving toward southeast (Figures 3b and 3d). From the analysis of CGPS velocities we can deduce that the ground deformation pattern affecting the Mt. Etna volcano at least since 2003 is clearly driven by two important mechanisms: 1) inflation/deflation cycles of volcanic origin, mainly revealed on the upper western flank; 2) a predominant southeastward movement of the eastern flank of the volcano, according to *Bonaccorso et al.* [2006] and *Bonforte et al.* [2008]. The kinematics of the eastern flank is the result of the interplay between the two different mechanisms. This last observation is not in agreement with the hypothesis of the wholly independent behavior of the entire eastern flank of the volcano, according to which the motion of the eastern flank would be unrelated to its magmatic and eruptive dynamics [*Bonforte and Puglisi*, 2003; *Bonforte et al.*, 2008, 2011], while the interplay between magmatic processes and the edifice spreading was already analyzed by *Lundgren et al.* [2004] by radar interferometry. The effects of the volcanic activities, of the gravitational loading and of the medium heterogeneities on the eastern flank were clearly shown by *Aloisi et al.* [2011b].

[29] Regarding the vertical velocities, Figure 4 highlights that: 1) a general subsidence is measured everywhere during eruptive periods, with higher subsidence rates in the summit areas (Figures 4b, 4d, and 4f); 2) a diffuse uplift is observed during recharging phases, except for the lower eastern flank, where the computed velocities are still negative (Figures 4a, 4c, and 4e). Therefore the whole lower eastern flank is marked by a general subsidence over the entire analyzed time interval, although this is not uniform and constant. This is evident if we compare the vertical velocities for the three analyzed inflation phases (Figures 4a, 4c, and 4e). Indeed, while the area affected by the subsidence is similar during the phases preceding the 2004–2005 and 2006 eruptions (although the subsidence rate is higher during the 2004–2005 pre-eruptive period) (Figures 4a and 4c), after the 2006 eruption the area affected by subsidence spread over the upper part of the volcano (Figure 4e). The higher negative values were measured along the North-East Rift zone (see EDAM and EMCN CGPS stations, Figure 4e) and near the northern sector of the Timpe fault system (see ESAL CGPS station, Figure 4e).

## 6. Analytical Models of the CGPS Data Recorded During the Inflation-Deflation Phases

[30] The surface displacement fields for each of the volcanic phase described in the previous paragraph were modeled to relate the observed crustal deformation patterns to pressure sources acting inside the volcano and to examine how pressure sources evolved. The modeled periods start with the inflation phase following the 2002–2003 eruption [e.g., *Aloisi et al.*, 2011b] and ends with the deflation phase accompanying the 2008 eruption [e.g., *Aloisi et al.*, 2009]. We used the entire CGPS network except the stations ECAN, ECNV and EPMN (Figure 1), which are located far outside the volcano edifice and that show a deformation pattern not directly linked to the volcanic dynamics but to a more broad scale tectonic deformation. Moreover, the lower eastern flank of the volcano is affected by an ESE-ward motion whose origin is still controversial and, as mentioned in the previous paragraph, is not always directly or simply correlated to the magmatic dynamics (for a summary, see sections 6 and 7 in *Aloisi et al.* [2011b] and reference therein). Therefore, for this modeling aimed at imaging the pressure magmatic sources exclusively, we did not take the GPS stations located on the lower eastern flank of the volcano (ELAC, ELEO, EPOZ and ESAL; Figure 1) into account. We verified that their use distorts the modeling solutions (see after). On the other hand, the mid-upper eastern flank shows both the effect of the volcanic processes (inflation/deflation phases) and the effect of a southeastern displacement. Therefore, the GPS stations located on the intermediate eastern flank (EMFN and EC10) were modeled during the deflation phases exclusively (Figures 3b, 3d, and 3f), because during the inflation phases they showed amplified displacements that were not coherent with the overall recorded deformation pattern (Figures 3a, 3c, and 3e). Finally, we did not use the EPDN data during the first phase (Figure 3a) and the EMCN data during the fifth phase (Figure 3e) since they were affected by local phenomena of anelastic displacements, most likely due to the proximity to volcanic fractures.

[31] We performed an analytical inversion of CGPS data, describing the pressure source with the arbitrarily oriented, finite, prolate and spheroidal cavity embedded in an elastic half-space of *Yang et al.* [1988]. We chose this source model among the other models published in literature [e.g., *Mogi*, 1958; *Davis*, 1986; *McTigue*, 1987] since, in this case, it shows a good trade-off between the number of degrees of freedom and the obtained data fit. The model of *Yang et al.* [1988] is determined by eight parameters: the coordinates $x_c$ and $y_c$ of the spheroid center, the coordinate $z_c$ of the spheroid center depth, the azimuth $\theta$ measured counterclockwise from the positive y direction around the z axis, the dipping angle $\phi$ measured clockwise from the positive y direction around the $x$ axis, the major semi-axis a, the ratio b/a between the minor and major axes, the intensity of the pressure P on the surface of the spheroid. The inversion was performed by using the Genetic Algorithms (GA) approach that solves nonlinear optimization problems using a global heuristics search [*Goldberg*, 1989]. Successively, starting

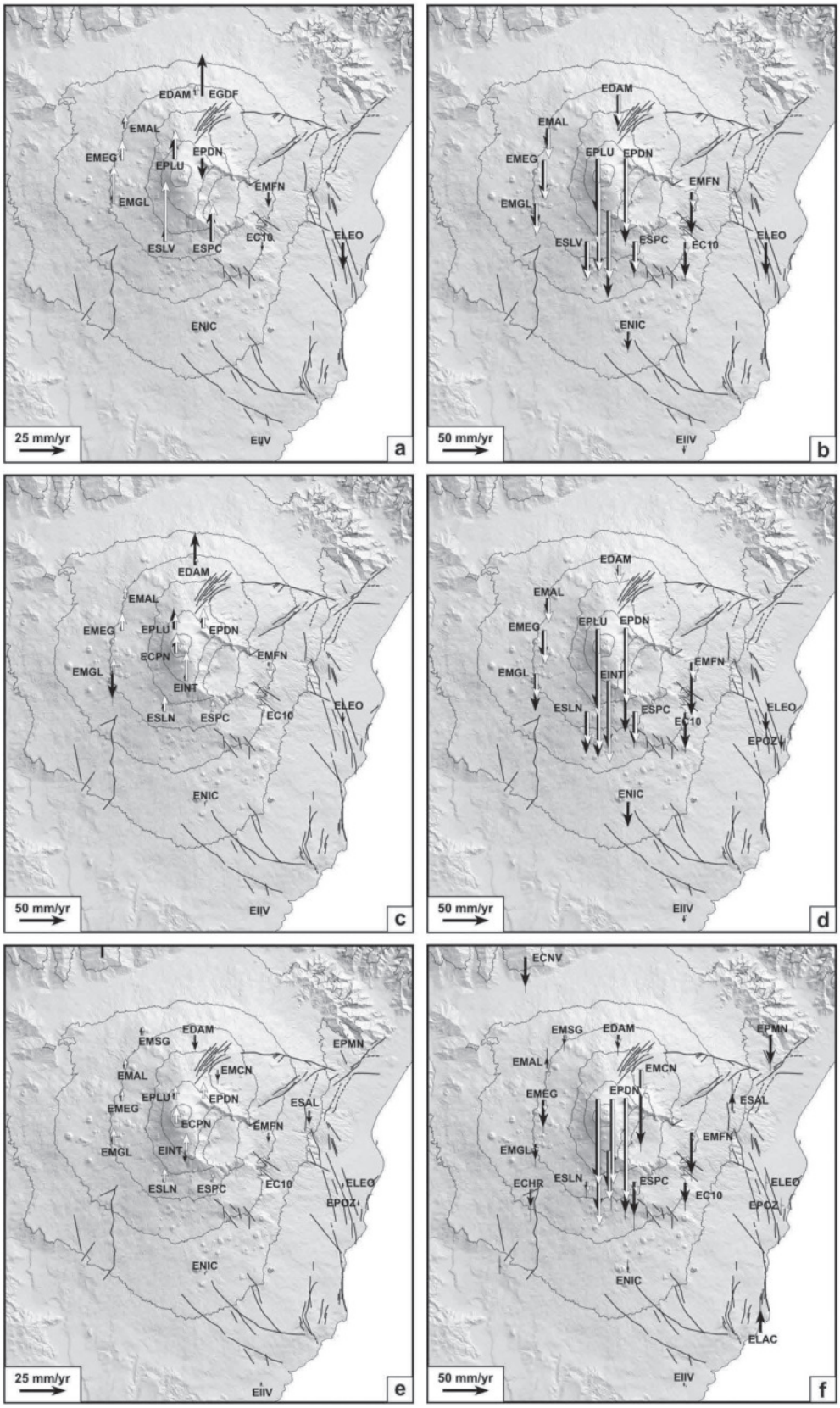


**Figure 4.** Observed vertical GPS velocities (black arrows) in the Etn@ref reference frame [*Palano et al.*, 2010] and modeled (white arrows) vertical velocities for each phase obtained using the *Yang et al.* [1988] model.

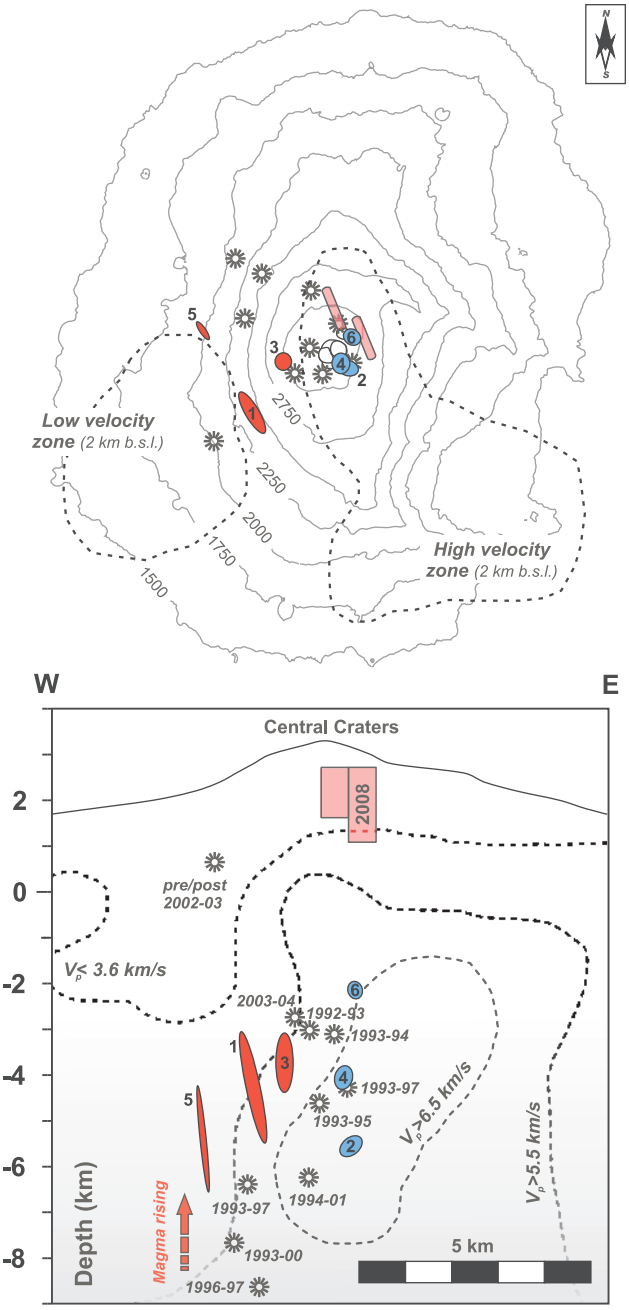


**Figure 5.** Pressure sources modeled for each phase (inflation in red and deflation in blue). The respective uncertainties of the location are also reported in light red or light blue. The surface and vertical projection of the modeled 2008 dike-forming intrusions [*Aloisi et al.*, 2009] is shown (light red). The consensus magma pathways (black asterisks) historically resolved by GPS, seismic and other geophysical data are indicated (see *Aloisi et al.* [2011a] for an overview). The trace of the high and low $v_p$ body estimated by *Aloisi et al.* [2002] is also shown. Redrawn by *Aloisi et al.* [2011a].

from the optimum solutions obtained using the GA approach, we applied the Pattern Search technique, which performs a search on a dynamic grid over the space of the source parameters [*Lewis and Torczon*, 1999]. Finally, to estimate the uncertainty of each optimized source parameter, a Jackknife re-sampling method [*Efron*, 1982] was adopted.

[32] We included the effects of the topography using the topographically corrected method of *Williams and Wadge* [2000]. This approach is a more precise method to model the combination of horizontal and vertical deformation with respect to the varying-depth model of *Williams and Wadge* [1998], which assumes a different elevation for each recording station corresponding to the relative elevation. It is noteworthy that, in our case, the *Williams and Wadge* [2000] approach provided deeper pressure sources of about 2 km with respect to the *Williams and Wadge* [1998] correction.

[33] Final optimal solutions for each phase are shown in Figure 5 and Table 1. The modeled and recorded deformation patterns are shown in Figure 3 and Figure 4. For all phases, we obtained a reduced chi-square equal to 1.0 considering the horizontal and vertical displacements with a value for the a-posteriori standard deviation of 0.016 m and 0.016 m, 0.006 m and 0.009 m, 0.015 m and 0.015 m, 0.003 m and 0.005 m, 0.005 m and 0.007 m, 0.004 m and 0.006 m, for the six phases respectively. Mainly for the two first inflations, the obtained uncertainties are bigger than the instrumental errors (few mm in the horizontal displacements and two or three times that in the vertical ones). We maintain that the remaining misfit is due to the use of a model that is still too simple with respect to a "volcano real model" because it does not consider, for example, a free shape for the deformation source but only a simple ellipsoidal shape. Moreover, our model does not account for the medium heterogeneities.

[34] Using a suitable value of the effective shear modulus $\mu$ for a hot volcanic region equal to 5 GPa [e.g., *Bonafede et al.*, 1986; *Davis*, 1986; *Bonaccorso et al.*, 2005], we calculated the volume change $\Delta V$ (Table 1) according to *Tiampo et al.* [2000]. Dividing the volume change $\Delta V$ by the duration of the phase, we estimated the inflation or the deflation rates for each phase (Table 1). The deflation rate can be usefully compared with the emission rate recorded during the eruptive periods (Table 1).

[35] Our results show a clear separation between the inflation and the deflation sources (Figure 5 and Table 1).

[36] The inflation sources are located, within 4.0 and 5.5 km (b.s.l.) and are characterized by an elongated shape. The maximum depth of the inflationary source can be associated to the minimal pressure at which volatiles (e.g., $H_2O$) are dissolved in magma with basaltic composition [cf. *Ferlito and Lanzafame*, 2010, and references therein].

[37] This depth could therefore be seen as critical, marking the beginning of the gas exsolution; we can therefore assume that the observed displacements are related to this process and, in particular, to the boiling of the water contained in the Etnean magmas. Moreover, our results show that the inflation pressure sources are located between the eastern border of the low velocity zone and the western border of the high velocity zone (Figure 5) found by *Aloisi et al.* [2002]. The low velocity-zone is located in the upper 3 km (b.s.l.) beneath the volcano's southwestern flank (Figure 5). This zone is aseismic and its location corresponds to the volume where the presence of a magma chamber was hypothesized on the basis of seismic b-value mapping [*Murru et al.*, 1999]. The domain below the low-velocity zone, bordering the high-velocity zone to the West [*Aloisi et al.*, 2002], is characterized by a

**Table 1.** Model Parameters and Related Uncertainties[a]

| Parameters | Phase 1 | Phase 2 | Phase 3 | Phase 4 | Phase 5 | Phase 6 |
|---|---|---|---|---|---|---|
| $x_c$ [m] | 497627 ± 501 | 500177 ± 408 | 498454 ± 125 | 499990 ± 160 | 496319 ± 345 | 500306 ± 344 |
| $y_c$ [m] | 4176647 ± 958 | 4177862 ± 895 | 4178038 ± 550 | 4178012 ± 180 | 4178864 ± 277 | 4178672 ± 494 |
| $z_c$ [m] | −4276 ± 1177 | −5598 ± 854 | −3781 ± 466 | −4102 ± 492 | −5443 ± 461 | −2134 ± 795 |
| $\theta$ [°] | 29 ± 76 | 70 ± 10 | 180 ± 9 | 118 ± 22 | 35 ± 70 | 33 ± 62 |
| $\phi$ [°] | 118 ± 29 | 35 ± 10 | 78 ± 90 | 56 ± 78 | 102 ± 12 | 132 ± 39 |
| a [m] | 1390 ± 261 | 339 ± 57 | 639 ± 99 | 283 ± 67 | 1261 ± 335 | 257 ± 92 |
| b/a | 0.111 ± 0.051 | 0.576 ± 0.078 | 0.341 ± 0.007 | 0.792 ± 0.126 | 0.056 ± 0.034 | 0.800 ± 0.141 |
| P [Pa] | 3.1E + 09 ± 7.0E + 08 | −7.7E + 09 ± 5.3E + 08 | 2.8E + 09 ± 5.4E + 08 | −3.1E + 09 ± 2.2E + 08 | 7.2E + 09 ± 6.1E + 08 | −1.5E + 09 ± 3.2E + 08 |
| ***$\Delta V$ [$m^3$]*** | ***6.5E + 07*** | ***−6.2E + 07*** | ***5.4E + 07*** | ***−2.8E + 07*** | ***2.9E + 07*** | ***−1.1E + 07*** |
| Duration [days] | 583 | 206 | 518 | 106 | 499 | 83 |
| Inflation versus deflation rate [$m^3$/s] | 1.3 | −3.5 | 1.2 | −3.0 | 0.7 | −1.5 |
| Emission rate [$m^3$/s] | | ∼2.7 (*) | | ∼2.2 (**) | | ∼1.5 (***) |
| Involved magma volume [$m^3$] | ***6.5E + 07*** | ***4.8E + 07*** | ***5.4E + 07*** | ***2.0E + 07*** | ***2.9E + 07*** | ***1.1E + 07*** |

[a]$\Delta$V is calculated according to *Tiampo et al.* [2000] using a value of the effective shear modulus $\mu$ equal to 5 GPa. The inflation and the deflation rates are calculated by dividing the volume change $\Delta$V by the respective phase duration. The involved magma volume regarding the inflation phases (phases 1, 3, and 5) is equal to the respective volume change $\Delta$V. Regarding the deflation phases (phases 2, 4, and 6), the involved magma volume is calculated as the arithmetic mean of the emission rate values provided by *Burton et al.* [2005], *Neri and Acocella* [2006a], and D. Andronico et al. (Morphostructural evolution and growth of the lava flow field during the 2004–05 eruption at Mt. Etna, submitted to *Journal of Volcanology and Geothermal Research*, 2011) for phase 2 (*), by *Behncke et al.* [2009] for phase 4 (**), and by D. Andronico (personal communication, 2011) for phase 6 (***), respectively. Rows with the estimated volume changes $\Delta V$ and the involved magma volumes are bolded for comparison.

high earthquake occurrence rate and it is considered a weakness zone with brittle behavior and a high degree of rock fracturing. It may be supposed that this zone includes paths for magma rising and stationing [*Aloisi et al.*, 2002]. In this framework, the area where we found the inflation pressure sources is compatible with the path along which the magma rises.

[38] The deflation pressure sources are located to the East with respect to the inflation sources, just below the Central Crater area (Figure 5). Unlike the inflation sources characterized by an elongated shape, the deflation sources showed an almost spherical shape. Moreover, they shift over time toward the volcano surface, from about 5.5 toward 2.0 km (b.s.l.).

[39] The calculated deflation rates are slightly higher than the recorded emission rates for the first two deflation phases but always compatible (Table 1). For the last deflation phase, we obtained the same values. Moreover, we obtained a progressive decrease of the involved magma volumes (Table 1). This coincides with the progressive decrease of the slope of the baseline during the recharging phases (Figure 2) and with the progressive shortening of the duration of the deflation phases (Figure 2).

[40] Finally, we performed some tests to verify the effect of the inclusion, in the modeling phase, of the stations located in the eastern flank. As already mentioned, we excluded the GPS stations of the Eastern flank (ELAC, ELEO, EPOZ and ESAL; Figure 1) because it is well known that the eastern flank is spreading seaward. The ground deformation pattern indicates that the displacement vectors are mainly oriented toward SE and South. The origin of this movement is still controversial and is most likely not always directly or simply correlated to the magmatic dynamics. Trying to explain the whole volcano deformation pattern, we performed an analytical inversion using contemporaneously an ellipsoidal pressure source [*Yang et al.*, 1988] and one of the deep detachment planes proposed in literature to take into account the strong motion recorded on the eastern flank [e.g., *Palano et al.*, 2008; *Puglisi et al.*, 2008]. The chosen detachment surface has the following characteristics: azimuth of N21°E, extension in depth from −1.4 km (b.s.l.) to −3.9 km (b.s.l.) with a dip angle of −11.6°, length of 26.4 km, width of 12.3 km. We always applied the *Williams and Wadge* [2000] topographical correction. We obtained volcanic sources sometimes much deeper than the solutions estimated excluding the motion of the eastern flank. Moreover, the fit of the stations located on the summit and on the intermediate altitudes worsened considerably. We maintain that this worsening is due to the use of an overly simple planar model to explain the really complex motion of the eastern flank whose dynamics, as aforementioned, is not uniquely interpreted and not directly linked to the magmatic dynamic that here we would model. Therefore, we retain that, the better choice to provide a suitable modeling of the magmatic sources is the exclusion of the eastern flank stations, as their use can severely distort the solutions.

## 7. Strain Rate Analysis

[41] In order to extend the knowledge of the crustal ground deformation pattern on Mt. Etna during the 2003–2008 time period, we have inverted the GPS velocities to model the strain rate fields.

[42] We have modeled the six periods discussed in the previous paragraphs by applying the method that was first described by *Haines and Holt* [1993], improved by *Holt and Haines* [1995] and explained and also used in other papers [e.g., *Haines et al.*, 1998; *Kreemer et al.*, 2000]. This methodology has already been widely applied to plate boundaries zone or seismogenic areas both on a regional and local scale [*Kreemer et al.*, 2000; *Beavan and Haines*, 2001; *Mattia et al.*, 2009, 2011] but represents a novelty in volcanic areas.

[43] The technique allows mapping geodetic velocities into a complete, horizontal velocity gradient tensor field within the investigated area. The velocity field $\mathbf{v}(\hat{x})$ is described by a rotation vector function $\mathbf{W}(\hat{x})$,

$$\mathbf{v}(\hat{x}) = r\mathbf{W}(\hat{x}) \times \hat{x}$$

where $\hat{x}$ is the unit radial position vector on the Earth's surface and $r$ is the radius of the Earth. The rotation vector function $\mathbf{W}(\hat{x})$ is expressed using a bicubic Bessel interpolation on a curvilinear grid [*Haines et al.*, 1998]. The horizontal strain rates, and the rotation rates about a vertical axis, are defined by expressions involving the spatial derivatives of the rotation vector function $\mathbf{W}(\hat{x})$.

[44] The optimal strain rate distribution, associated with the GPS velocities, is obtained through the minimization of the following functional in a formal least squares inversion

$$\chi = \sum_{cells}\sum_{ij,kl}\left(\bar{\dot{e}}_{ij}\right)^T \mathbf{V}_{ij,kl}{}^{-1}\left(\bar{\dot{e}}_{kl}\right) + \sum_{knots}\sum_{i,j}\left(\bar{v}_i - \bar{v}_i{}^{obs}\right)^T \mathbf{V}_{i,j}{}^{-1}\left(\bar{v}_j - \bar{v}_j{}^{obs}\right),$$

where $\mathbf{V}_{ij,kl}$ is the variance-covariance matrix of the expected strain rates, $\mathbf{V}_{i,j}$ is the variance-covariance of the GPS velocities, $\bar{v}_i{}^{obs}$, and $\bar{v}_i$ and $\bar{\dot{e}}_{ij}$ are the model values of velocity and strain rate, respectively. We use an adjustable isotropic component of strain rate variance, embedded in $\mathbf{V}_{ij,kl}$, as a measure of the a priori expected departure of strain rates from a long-term secular field. Such a departure would be a transient associated with volcanic inflation or deflation. This isotropic component of variance is adjusted until the reduced Chi-square misfit to the GPS velocities is optimal (around 1.0). This single adjustable parameter is isotropic, and constant everywhere, because there is no a priori expectation on the style or distribution of potential strain rate transient associated with volcanic deformation. The optimization of the functional provides a minimum in the second invariant of the model strain rates, normalized by the a priori variance-covariances, while also providing a minimum in misfit to the GPS (reduced Chi-square misfit of 1.0).

[45] We have designed a grid region surrounding Mt. Etna where we were able to model the CGPS data and we experimented with different grid sizes in order to maximize the resolution for the given station spacing. The model is calculated on a regular 0.05° × 0.05° grid, whose nodes do not coincide with any of the geodetic monuments and which extends from a longitude of 14.80° to 15.25° and a latitude of 37.50° to 37.90° (Figure 1). The model parameters shown in this paper are continuous areal strain rates, shear strain

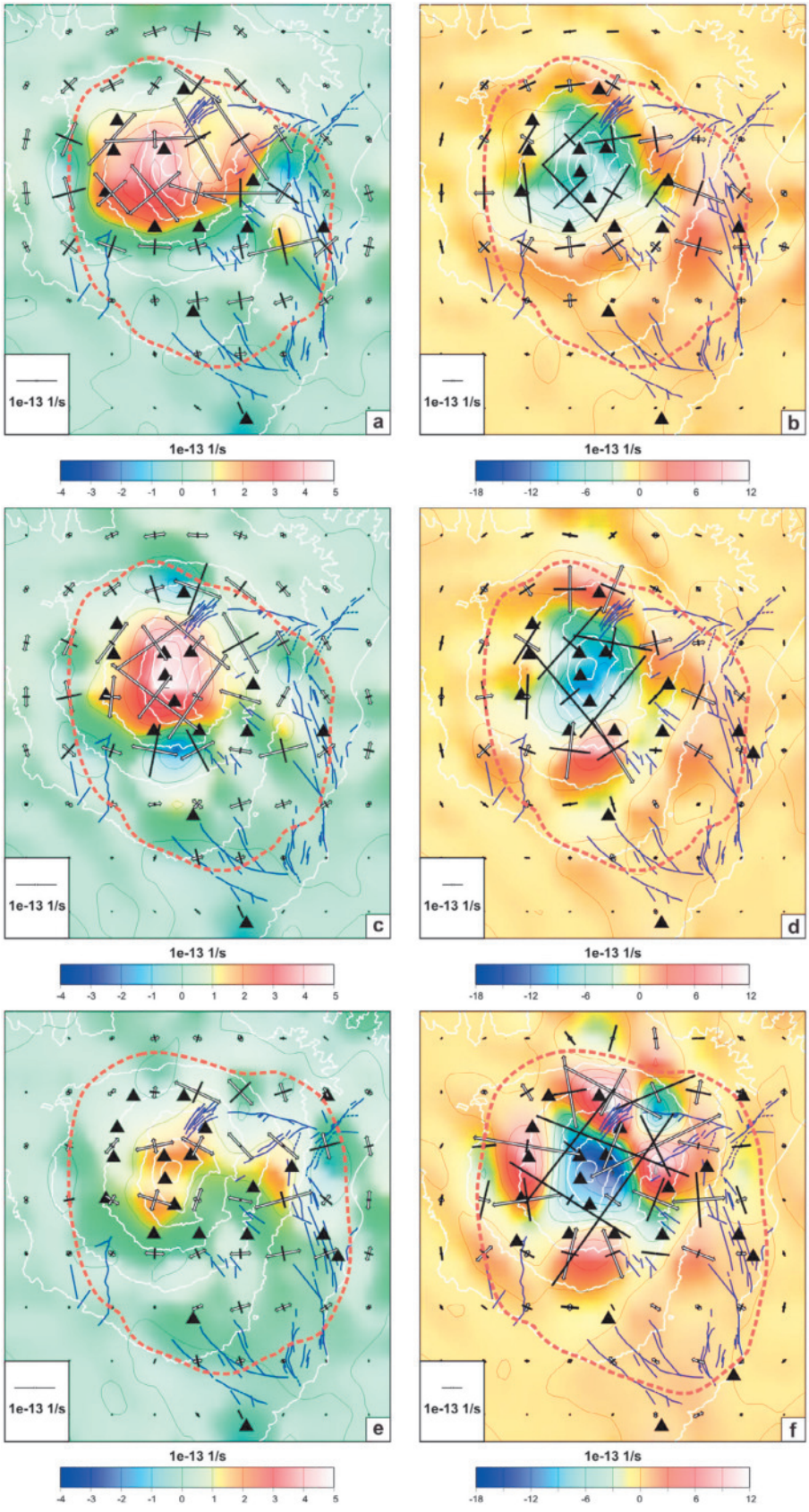
1e-13 1/s
a
1e-13 1/s
-4 -3 -2 -1 0 1 2 3 4 5
1e-13 1/s
b
1e-13 1/s
-18 -12 -6 0 6 12
1e-13 1/s
c
1e-13 1/s
-4 -3 -2 -1 0 1 2 3 4 5
1e-13 1/s
d
1e-13 1/s
-18 -12 -6 0 6 12
1e-13 1/s
e
1e-13 1/s
-4 -3 -2 -1 0 1 2 3 4 5
1e-13 1/s
f
1e-13 1/s
-18 -12 -6 0 6 12

**Figure 6**

rate magnitudes associated with a strike-slip component of deformation and rotation rates. We have calculated area averages (within grid cells) of these quantities and the a posteriori model uncertainties and model resolution.

[46] We used the whole CGPS network except the stations ECAN and ECNV (Figure 1), which are located far outside the volcano edifice, while we considered the station EPMN in the inversion that could be useful to eventually investigate the change in deformation style observed across the Pernicana Fault System (Figure 1) [*Palano et al.*, 2009; *Bonforte et al.*, 2011]. Moreover, unlike the procedure of volcanic source modeling (see previous section), we took into account the GPS stations located on the lower eastern flank of the volcano (Figure 1) as we are interested in studying the crustal ground deformation of the entire volcanic edifice. Thus, comparing the observed strain fields with the synthetic strain fields, as calculated starting from theoretical velocities maps obtained from the modeled volcanic sources (Table 1), we are able to accurately investigate the areas where non-volcanic processes are predominant.

### 7.1. Strain Rate Fields and Rotation Rates at Mt. Etna

[47] In Figure 6 we plot the areal strain rates together with the principal axes of the average strain rates within each $0.05^\circ \times 0.05^\circ$ area. The increasing number of CGPS stations over the analyzed time period has allowed an improvement of the resolution of the model strain rate fields over time, computed as in *Kreemer et al.* [2000] and reported as red dotted lines, which mark off the area with a greater than 50% level resolution.

[48] Figures 6a and 6c show that the inflation phases are dominated by areal dilatations that spread out over the upper part of the volcano, around the summit craters and are bounded by zones of minor contraction on the more distant flanks of the volcano, with radially directed principal axes of compression. In the first phase (Figure 6a) the areal dilatation extends greater to the North–East, bounded to the North by the Pernicana fault system and the North-East Rift. The higher extensional strain rates were computed roughly perpendicular to the North-East Rift, reaching values of about $2–2.5 \cdot 10^{-13}$ 1/s (Figure 6a), thus reflecting the presence of subsurface stress acting along these structures.

[49] The highest positive areal strain rate values are reached in the second recharge phase along the summit craters area (Figure 6c), where we measure values of about $5 \cdot 10^{-13}$ 1/s.

[50] As already shown with the analysis of the horizontal and vertical velocity fields, the inflation that preceded the 2008 eruption has a different behavior (Figure 6e) with respect to the first two recharge phases. We measure areal dilatation rates that do not exceed $2 \cdot 10^{-13}$ 1/s from the summit craters to the mid-upper eastern flank, up to the ESAL CGPS station.

[51] The eruptions are accompanied by higher deformation rates with respect to the inflation periods. An evident feature in the areal strain rate during eruptive phases is a general strong contraction that characterizes the summit area of the volcanic edifice (Figures 6b, 6d, and 6f), accompanied by dilatations that affect the remaining part of the volcanic edifice. The pattern of the areal strain rate is very similar during the 2004–2005 and 2006 eruptions (Figures 6b and 6d), although a more intense extension along the eastern flank is measured during the 2004–2005 eruption (Figure 6b).

[52] The last deflation phase, associated to the 2008 eruption, has a different areal strain rate pattern (Figure 6f). It is characterized by the highest contractional strain rate along the summit area with values of about $-18 \cdot 10^{-13}$ 1/s. This area is surrounded by an intense areal dilatation that reaches values of about $12 \cdot 10^{-13}$ 1/s along the North-East Rift and the mid-upper eastern flank of Mt. Etna (Figure 6f).

[53] The strain rate analysis has also allowed detecting geodetic rotations in the Etnean area (Figure 7). They are not the same during the investigated time period but vary from one volcanic phase to another, although some features are common to different periods.

[54] During the recharge phases (Figures 7a, 7c, and 7e) we can observe areas of clockwise rotation measured along the upper eastern flank that disappear during deflation phases. The maximum clockwise rotation rates are computed before the 2004–2005 and the 2006 eruptions, reaching values of about $2.5 \cdot 10^{-13}$ rad/s (Figures 7a and 7c), while they are less impressive during the recharge phase that preceded the 2008 eruption (Figure 7e). The clockwise rotations extend from the summit craters during the first inflation phase and from the upper eastern flank during the second and third ones, and are bounded approximately to the North by the North-East Rift and the Pernicana fault system, to the North-East by the Ripe della Naca fault scarps and to the East by the Timpe fault system (Figures 7a, 7c, and 7e).

[55] The rotation rates indicate the following: 1) the area affected by clockwise rotation has a low internal shear strain rate (Figures 8a, 8c, and 8e), whereas the bounding areas or faults are characterized by higher shear strain rates values (see next paragraph for more details), as we might expect for a crustal rotation; 2) they concur with the area of clockwise rotation found by *Solaro et al.* [2010]; 3) they are compatible with the dip-slip displacements coupled with left-lateral components revealed along the Pernicana fault system [*Azzaro* 1997, 2004] and with the indication of this structure as a left-lateral shear zone [*Groppelli and Tibaldi*, 1999; *Aloisi et al.*, 2011b].

### 7.2. Comparison Between Geodetic Strain Rate, Synthetic Strain Rate Fields by Modeled Volcanic Sources and Seismic Energy Release

[56] The strain rate analysis also allows inferences to be made about earthquake hazard assessment [*Beavan and Haines*, 2001]. Starting from this assumption, we wish to see how the strain rates inferred from GPS observations compare with the seismic energy release around Mt. Etna

**Figure 6.** Areal strain rates together with the principal axes of the average strain rates within the $0.05^\circ \times 0.05^\circ$ grid areas. Open arrows indicate extensional strain rates and solid arrows correspond to compressional strain rates. Note the factor of change in strain rate scale between the (a, c, and e) inflation and (b, d, and f) deflation phases due to the high increase of deformation rate during eruptive periods. The resolution of the strain rate fields [*Kreemer et al.*, 2000] are reported as red dotted lines, which mark off the areas with a greater than 50% resolution level.

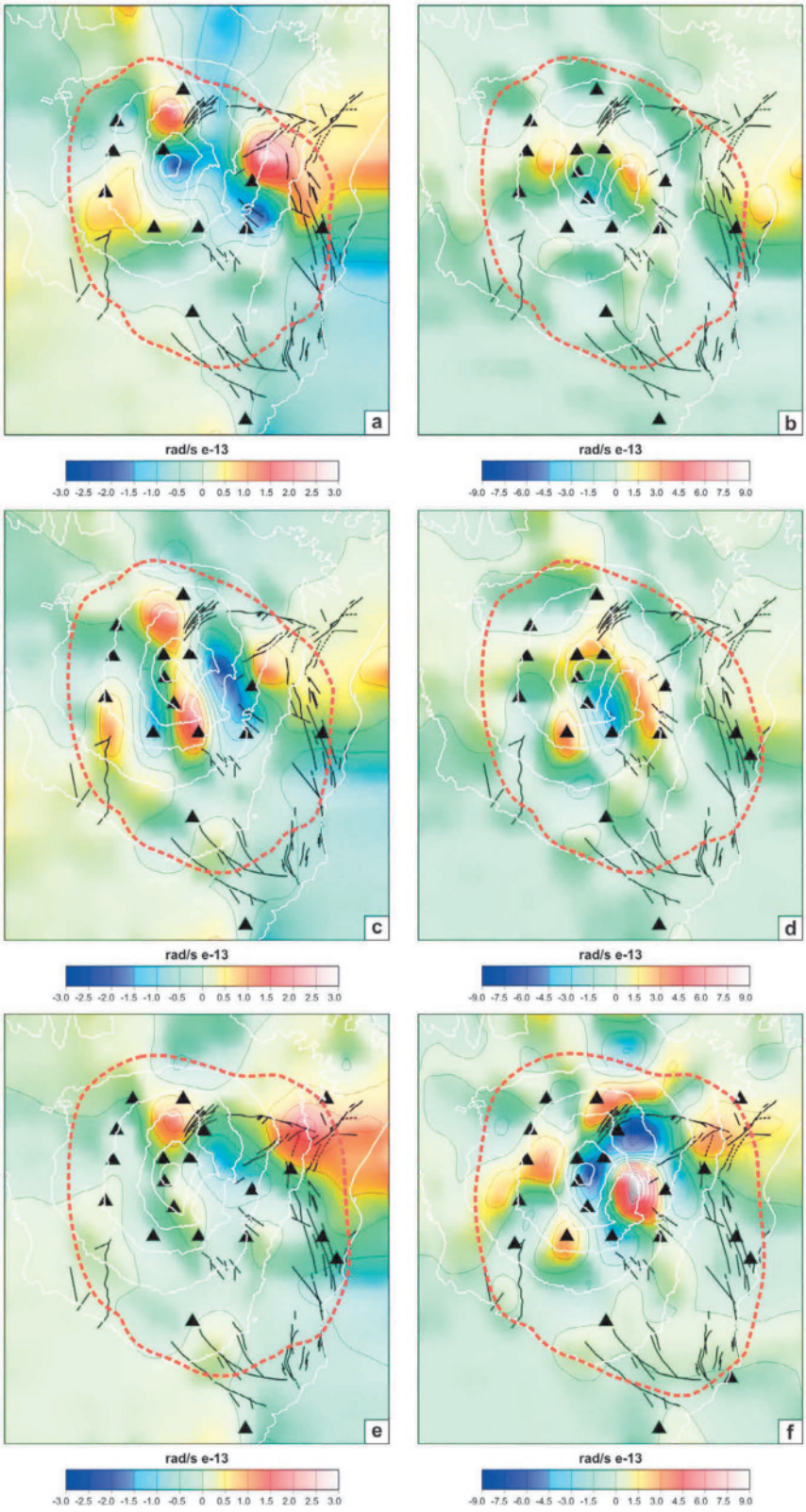


**Figure 7.** Geodetic rotation rates. Negative values indicate clockwise rotations while positive values represent counter-clockwise rotations. Note the factor of change in the scale between the (a, c, and e) inflation and (b, d, and f) deflation phases. The resolutions of the images [*Kreemer et al.*, 2000] are reported as red dotted lines, which mark off the area with a greater than 50% resolution level.

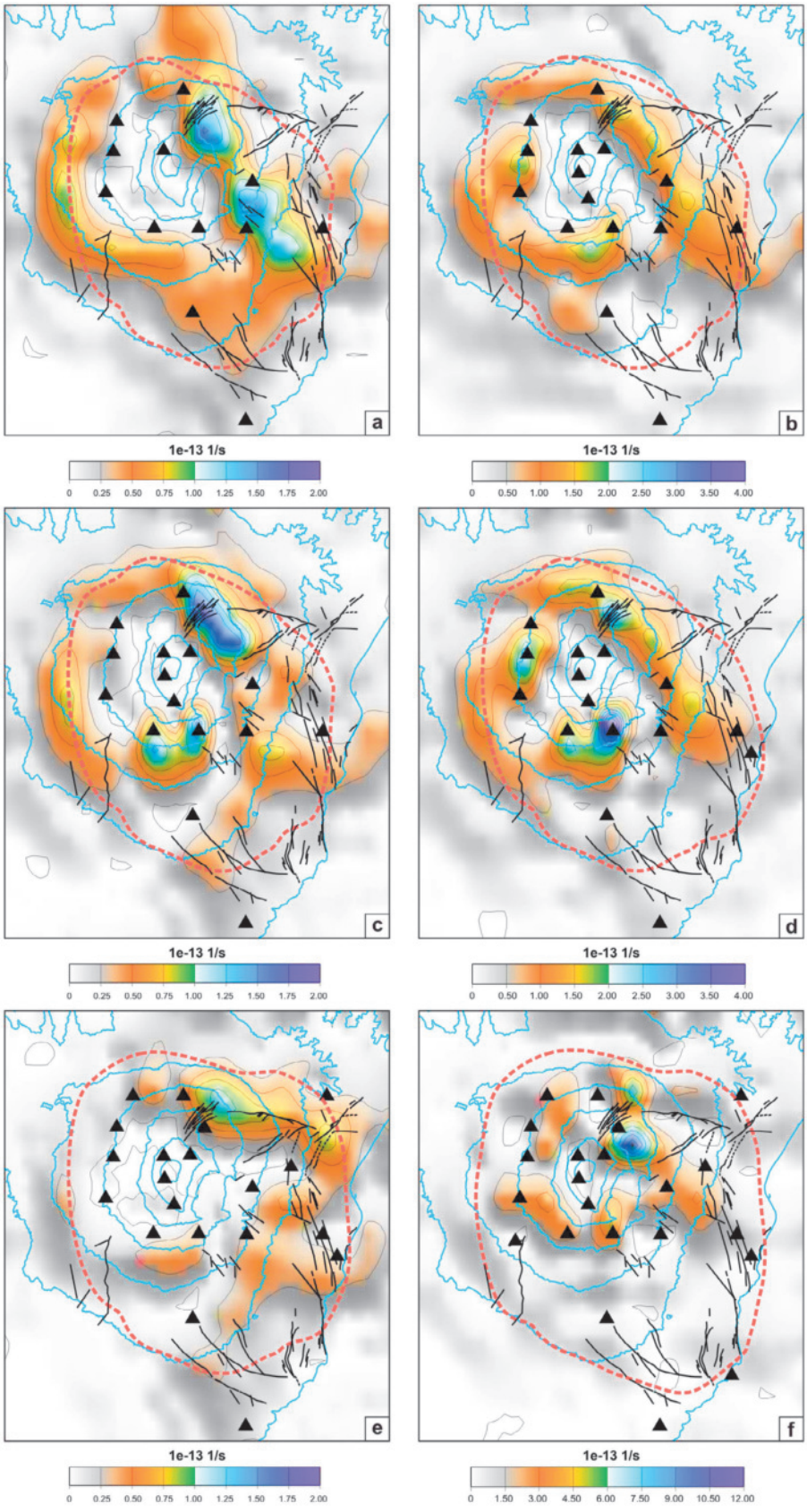
a
1e-13 1/s
0 0.25 0.50 0.75 1.00 1.25 1.50 1.75 2.00
b
1e-13 1/s
0 0.50 1.00 1.50 2.00 2.50 3.00 3.50 4.00
c
1e-13 1/s
0 0.25 0.50 0.75 1.00 1.25 1.50 1.75 2.00
d
1e-13 1/s
0 0.50 1.00 1.50 2.00 2.50 3.00 3.50 4.00
e
1e-13 1/s
0 0.25 0.50 0.75 1.00 1.25 1.50 1.75 2.00
f
1e-13 1/s
0 1.50 3.00 4.50 6.00 7.50 9.00 10.50 12.00

**Figure 8**

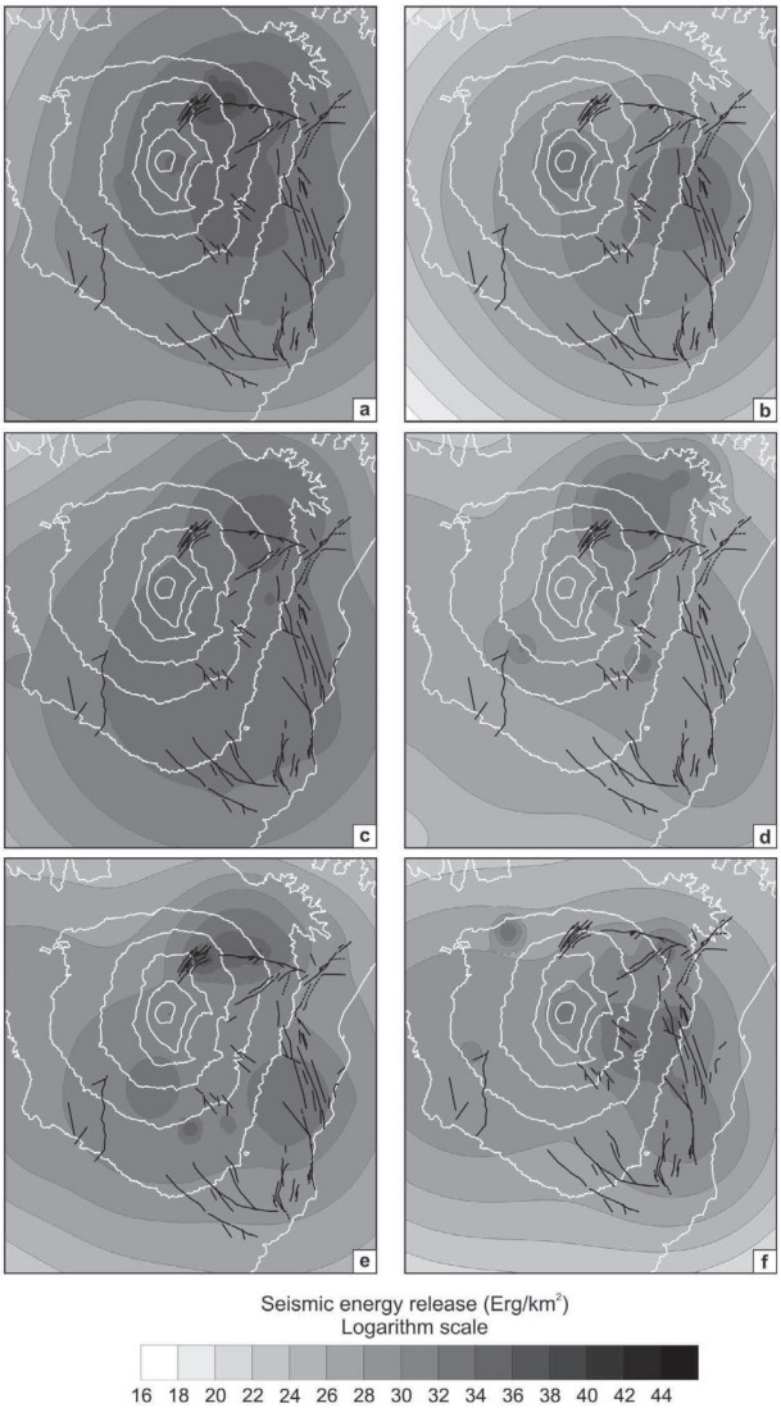


**Figure 9.** Seismic energy release expressed in logarithm scale for each different phase.

**Figure 8.** Magnitude of geodetic shear strain rate associated with the component of the strain tensor field that has a pure strike-slip style of deformation (equal magnitudes of compression and extension principal axes). Note the factor of change in the scale between the (a, c, and e) inflation and (b, d, and f) deflation phases. The scale used for the last deflation phase (Figure 8f) is different from the other two phases, due to the high shear strain rate values. The 50% resolution levels of the maps [*Kreemer et al.*, 2000] are reported as red dotted lines.

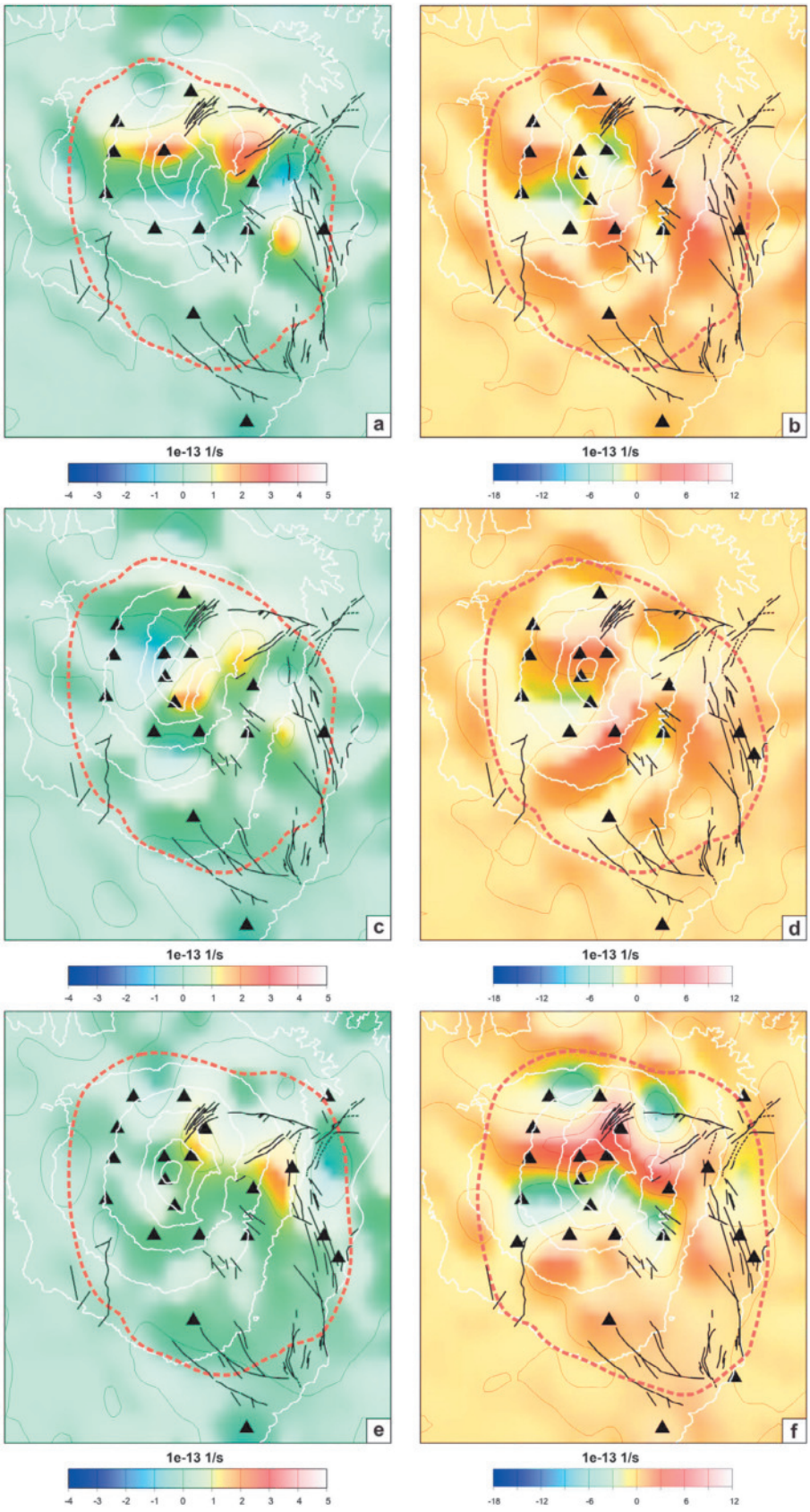
a
1e-13 1/s
-4 -3 -2 -1 0 1 2 3 4 5
b
1e-13 1/s
-18 -12 -6 0 6 12
c
1e-13 1/s
-4 -3 -2 -1 0 1 2 3 4 5
d
1e-13 1/s
-18 -12 -6 0 6 12
e
1e-13 1/s
-4 -3 -2 -1 0 1 2 3 4 5
f
1e-13 1/s
-18 -12 -6 0 6 12

**Figure 10**

and try to understand if strain rate maps could provide information regarding the occurrence of seismic activity at Mt. Etna.

[57] In order to compare the geodetic strain rate with the seismicity we calculated the maps of the seismic energy release for each considered time period (Figure 9). To this end, we took into account the instrumental seismicity recorded in the Etnean area from the INGV-CT catalog (available at http://www.ct.ingv.it/ufs/analisti/catalogolist.php) where the earthquake locations are performed by using the software Hypoellipse 2.0 [*Lahr*, 1989] and the crustal velocity model reported in *Hirn et al.* [1991]. In particular, we only took into account the earthquakes related with the volcano activity by filtering out the deeper events and considering just the shallow earthquakes with a hypocentral depth between −3 and 5 km b.s.l.

[58] According to *Maaz et al.* [1974], we calculated, on an equispaced grid (step 0.01°) covering the whole area, the cumulative quantity:

$$S_r[P] = \sum_Q S_r[P,Q] = \sum_Q \frac{E}{4\pi h^2} \exp\left[-\left(\frac{\Delta}{2h}\right)^2\right]$$

where Q is a shallow earthquake (with maximum depth of 5 km) occurring in the considered period, h its depth, E its energy and $\Delta$ is the epicentral distance to the point of computation *P*. The earthquake energy is linked to its magnitude according to *Gutenberg and Richter* [1956] by the equation:

$$\log E = 11.8 + 1.5\,M$$

Figure 9 shows that higher seismic energy releases occur along the eastern flank of the volcanic edifice. In particular, the highest values of about 32 Erg/km$^2$ are measured along the North-East Rift, the Pernicana fault system and the Timpe fault system. It is interesting to note the good agreement between seismic energy release (Figure 9) and geodetic shear strain rate (Figure 8), mainly during the inflation phases. Note that Figure 8 represents the magnitude of the component of the strain rates that would accommodate pure strike-slip faulting (equal magnitude of compressive and extensional principal axes). The only areas in which there is not a good correspondence are the summit craters and the upper sector of the western flank, where nevertheless the geodetic strain rates appear as areal dilatation or compression (Figure 6).

[59] By analyzing the first two recharge phases of the volcanic edifice we can notice the presence of a belt of shear strain rate which extends from the North–East Rift to the Santa Venerina fault and the Timpe fault system, along a NNW-SSE direction, roughly parallel to the Timpe fault system (Figures 8a and 8c). This belt reaches shear strain rate values of about $1.5 \cdot 10^{-13}$ 1/s, mostly along the North-East Rift. Furthermore, we can observe a propagation of the shear strain along the Pernicana fault system during the phase that preceded the 2008 eruption (Figure 8e), in agreement with the seismic energy release (Figure 9e).

[60] These features also remain visible if we remove the crustal deformations due to the pressure magmatic sources acting inside the volcano. For this reason, we have computed synthetic strain rate fields starting from theoretical velocity maps obtained from the modeled volcanic sources (see paragraph 7). The synthetic strain rate fields have been subtracted from the strain rate fields obtained from the inversion of the computed GPS velocities and results are reported in Figure 10 and in Figure 11, as areal strain rates and shear strain rates respectively. We can observe that the areal strain rate values are heavily reduced (Figures 6 and 10). This means that they are mainly related to inflation and deflation sources. The shear strain rates instead remain very similar during the inflation phases (Figures 8a, 8c, 8e, 11a, 11c, and 11e). The only differences are represented by the shear strain rates computed along the western flank of Mt. Etna volcano. They disappear after the removing of crustal deformation due to modeled pressure sources (Figure 11), thus implicating a dependency on processes acting inside the volcano. The dependency on inflation sources is instead very small during the phase that preceded the 2008 eruption, as the shear strain rate pattern of the entire volcanic edifice remains almost unchanged after the removing of the effect due to magmatic source (Figures 8e and 11e). Therefore, we can deduce that the synthetic shear strain rate patterns (Figure 11), mostly concentrated along the eastern flank of Mt. Etna, could be due to non-volcanic processes.

## 8. Discussion and Conclusive Remarks

[61] The main aim of this work was the investigation of the volcanic sources acting beneath Mt. Etna and their role in the complex pattern of ground deformation measured by a dense network of CGPS stations between 2003 and 2008.

[62] The analysis has allowed highlighting the presence of inflation/deflation cycles of the volcanic edifice. Many authors have proposed the existence of different categories of cyclic patterns both in long and short-term eruptive behavior of Etna [*Imbò*, 1928; *Wadge et al.*, 1975; *Guest and Murray*, 1979; *Behncke and Neri*, 2003]. *Branca and Del Carlo* [2005], on the contrary, ruled out cyclic behavior of Etna, arguing that the activity of the volcano has been increasing during the past few decades, although *Allard et al.* [2006] suggested that the recent increase in activity may only have accelerated the succession of the different phases of an eruptive cycle. The choice of the period here analyzed is not incidental. According to our data, though we cannot comment on the long-term behavior of the volcano, we maintain that there is a possible interpretation of this time span as a small scale cycle occurring between two eruptions characterized by forceful intrusions of dikes (2002–03 and 2008).

[63] During the 2003–2008 eruptive cycle, in our view, the emission of magma from the summit craters or from fractures close to the main craters represents a phase of transition

**Figure 10.** Residual areal strain rates obtained by subtracting from the strain rate fields, obtained from the inversion of the computed GPS velocities (Figure 6), synthetic strain rate fields, calculated from theoretical velocities obtained from the modeled active sources. Note the factor of change in strain rate scale between the (a, c, and e) inflation and (b, d, and f) deflation phases due to the high increase of deformation rate during eruptive periods. The 50% level resolutions of the maps [*Kreemer et al.*, 2000] are also reported as red dotted lines.

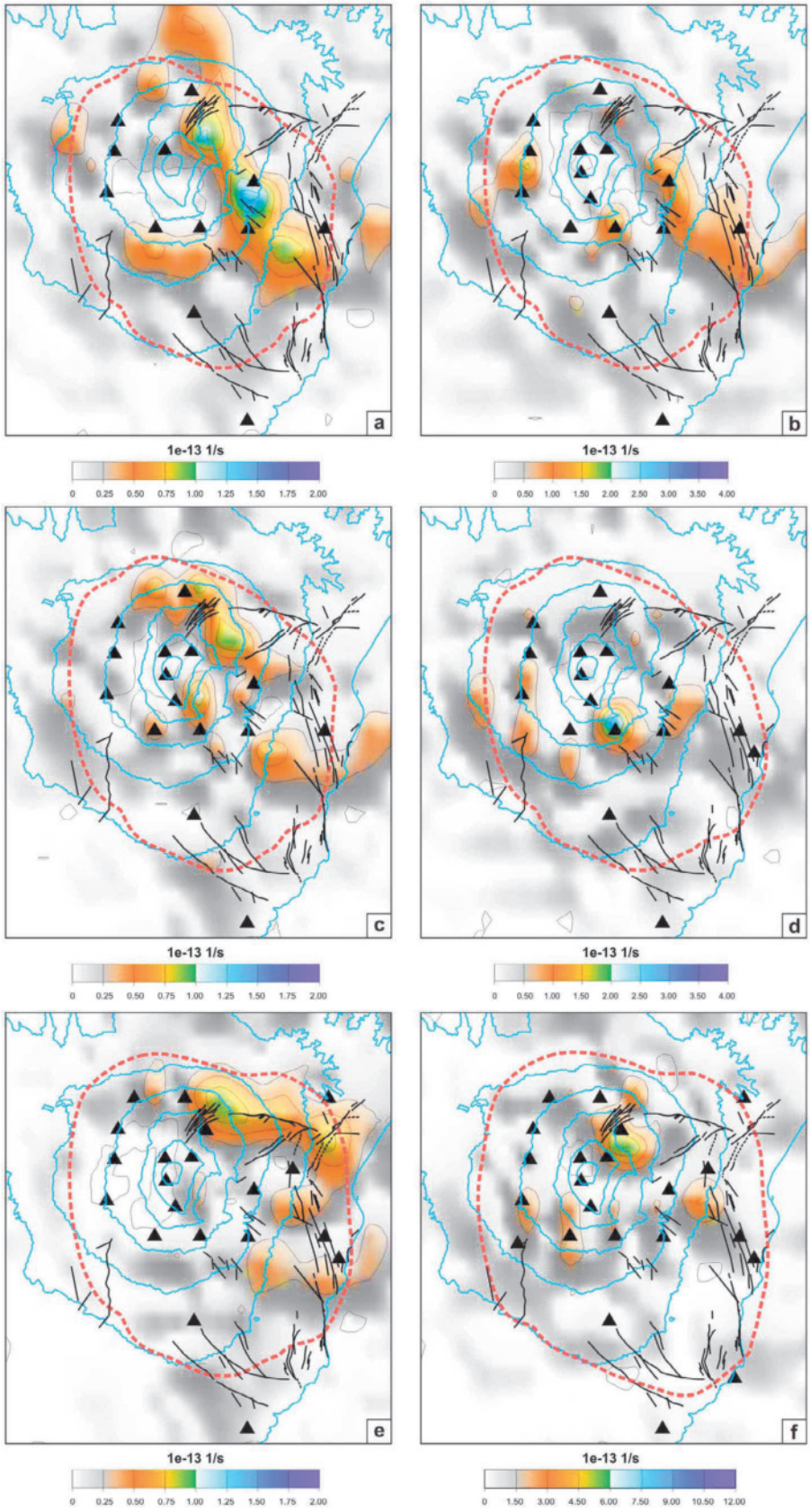
a
1e-13 1/s
0 0.25 0.50 0.75 1.00 1.25 1.50 1.75 2.00
b
1e-13 1/s
0 0.50 1.00 1.50 2.00 2.50 3.00 3.50 4.00
c
1e-13 1/s
0 0.25 0.50 0.75 1.00 1.25 1.50 1.75 2.00
d
1e-13 1/s
0 0.50 1.00 1.50 2.00 2.50 3.00 3.50 4.00
e
1e-13 1/s
0 0.25 0.50 0.75 1.00 1.25 1.50 1.75 2.00
f
1e-13 1/s
0 1.50 3.00 4.50 6.00 7.50 9.00 10.50 12.00

**Figure 11**

during which magma enriches its content in volatile components. This aspect is demonstrated by the progressive decrease of the involved magma volumes (Table 1), mainly in the last phase. It corresponds with: 1) a progressive decrease of the slope of the EMAL-EMGL baseline during the inflation phases; 2) smaller GPS velocities for the last inflation preceding the 2008 eruption. This behavior could be explained by considering the role of the volatiles content in magma [*Aloisi et al.*, 2011a]. In this framework, the progressive shallowing of the deflation sources is another key point which demonstrates that between 2003 and 2008 we have geodetically measured the effects of complex processes where a primary role is played by the volatiles.

[64] *Aloisi et al.* [2011a] have modeled an elongated plumbing system beneath Mt. Etna using CGPS data. Other authors have excluded the presence of large-scale crustal reservoirs beneath Mt. Etna [e.g., *Corsaro and Pompilio*, 2004, and references therein]. If the model proposed in *Aloisi et al.* [2011a] is valid, we have observed a progressive enrichment of fluids during the period 2003–2008 that progressively involved the elongated plumbing system, which was filled by magma depleted in volatiles by the 2001 and 2002–2003 eruptions.

[65] During the 2004 eruption, the arrival of new magma enriched in volatiles content (also testified by petrological data) drove the remaining old magma still residing in the shallowest part of the plumbing system and, in 2006 and 2007, it produced sporadic, but strongly explosive, manifestations of volcanic activity where small quantities of such "volatile-rich" magma were involved.

[66] During these eruptions, the loss of magma caused the fast decompression that produced an increase in the rate of volatile exsolution in a reservoir located between 2000 and 3000 m b.s.l., which led to a final forceful intrusion during the 2008–2009 eruption that ended the cycle.

[67] The position of the inflation pressure sources is compatible with the path where the magma is supposed to rise, according to the tomographic analysis of *Aloisi et al.* [2002]. Moreover, the progressive shallowing of the deflation sources could be due to the elongated plumbing system depressurizing at ever more shallow levels. Such a depressurization is also accompanied by decreasing values of the magma volumes calculated in our models (Table 1). It is important to stress the importance of the "inflating body" revealed by our models (Figure 5), that is almost the same (considering the errors in the estimation of its position) during the whole 2003–2008 period. This level, observed also by other geophysical investigations [*Aloisi et al.*, 2011b, 2002], is of primary importance because, considering its depth beneath the crater area of Mt. Etna (about 7 km), it corresponds to the pressure of exsolution (180 Mp) and bubbles formation of Etnean magmas with a normal content in water (2%).

[68] *Mastin et al.* [2008; 2009] have clearly shown that the volumes of magma obtained from the inversion of geodetic data measured during the deflation which occurred after the 2004–05 eruption at Mt. St. Helens are lower than the volumes emitted during the eruption. These authors have also demonstrated that this difference is the expected consequence of the finite compressibility of the magma and it is not necessarily due to an almost continuous intrusion of new magma in the shallow reservoir. The context of Mt. Etna is different with respect to Mt. St. Helens (basaltic versus silicic magma; an elongated and multilevel plumbing system versus a magma chamber; a typical effusive basaltic volcano versus an explosive one) and we can define some interesting differences. The most important is that, at Mt. Etna, there is no significant difference between the volumes of magma estimated for the deflation phases and the emitted ones, considering the errors in both the values (Table 1). This means that the compressibility of magma does not play an important role at Mt. Etna and confirms the absence of any large magma reservoir. *Mastin et al.* [2009] define the volcanic system of Mt. St. Helens as "resilient and dynamic." On the contrary, Mt. Etna appears to be poorly resilient (every variation due to the recharge-discharge phase induces significant variations that potentially lead to a new eruptive phase) and highly dynamic.

[69] We have also demonstrated that the kinematics and the ground deformation pattern observed on Mt. Etna are not only due to magmatic sources acting inside the volcano, but are strongly influenced by the southeastward motion of the eastern flank of the volcano. Nevertheless, while the kinematics of the northern, western, southern and upper eastern flank of the volcano and of its summit area is mainly controlled (for the considered time span) by the magmatic sources acting inside the volcano, the mid-upper eastern flank is clearly driven by the interplay between the two different components. Furthermore, the southeastward directed motion prevails over the effects due to magmatic sources in the lower eastern flank.

[70] These results are also confirmed by the analysis of the strain rate maps. Indeed, the comparison between the strain rate patterns, before and after the removing of the effect of the modeled magmatic sources, shows that the dilatation strain rates remain unchanged in the lower eastern flank and the shear strain is approximately the same along the entire eastern flank, while the strain rate values undergo heavy reductions on the rest of the volcanic edifice. Although these results were expected after the exclusion from the modeling of the volcanic sources of the CGPS stations located in the lower part of the eastern flank, they highlight the different behavior of the eastern flank with respect to the rest of the volcanic edifice and permit a first quantification and detailed analysis of the strain acting in this important sector of the volcano.

[71] Our modeling of the geodetic velocity field has allowed us to precisely pinpoint an area of clockwise rotation rates (Figure 7), which extends in the eastern flank,

**Figure 11.** Residual geodetic shear strain rates obtained by subtracting from the shear strain rate fields, obtained from the inversion of the computed GPS velocities (Figure 8), synthetic shear strain rate fields, calculated from theoretical velocities obtained from the modeled active sources. Note the factor of change in the scale between the (a, c, and e) inflation and (b, d, and f) deflation phases. The scale used for the last deflation phase (Figure 11f) is different from the other two phases, due to the high shear strain rate values. The 50% level resolutions of the maps [*Kreemer et al.*, 2000] are also reported as red dotted lines.

bounded approximately to the North by the North-East Rift and the Pernicana fault system, to the North-East by the Ripe della Naca fault scarps and to the East by the Timpe fault system. This feature is compatible with the area of clockwise rotation found by *Solaro et al.* [2010] and with left-lateral components revealed along the Pernicana fault system [*Azzaro*, 1997, 2004; *Aloisi et al.*, 2011b]. It is also interesting to note the good agreement between the area affected by higher seismic energy release and higher geodetic shear strain values, mainly during the inflation phases. The only areas in which there is not a good correspondence are the summit craters and the upper sector of the western flank, where nevertheless the geodetic strain rates appear as areal dilatation or compression. This is a potentially important result since it means that geodetic shear strain rate distribution can provide useful information regarding the future occurrence of seismic activity at Mt. Etna.

[72] Finally, the strain rate analysis has allowed a highlighting of the different deformation behavior of the 2008 pre-eruptive period with respect to the inflation phases preceding the 2004–2005 and 2006 eruptions. Both the dilatation and the shear strain rate patterns confirm that the deformations that preceded the 2008 eruption were less impressive than the other recharge periods. Our results indicate a propagation of the shear strain rates along the Pernicana fault system that is not present in the previous phases. This result is accompanied by the enlargement of the area of the eastern flank involved in the subsidence, which spread over the upper part of the volcano, and by a decrease in its clockwise rotation rate.

[73] In conclusion, in this work we have proposed an analysis of the geodetically observed ground deformation pattern at Mt. Etna for the period 2003–2008. We have found some interesting aspects that should be explored in the near future, also considering the ever-growing number of CGPS stations along the slopes of the volcano. We used a dual-method approach: the inversion of the geodetic data to determine the volcanic sources and the strain rate maps in order to image both tectonic and volcanic effects. The main results can be summarized in a few points: 1) The study of the cycle between two eruptions characterized by the forceful intrusion of magma has revealed a process of almost continuous enrichment of volatile content of the involved magma; 2) the strain rate analysis applied to volcano monitoring has emphasized its importance in summarizing, in a simplified way, the large amount of information derived from the GPS velocity fields. This importance is especially evident with the observation that seismicity takes place where the highest values of shear strain rates occur. Furthermore, the joint use of the strain rate maps with the modeling of pressure sources acting inside the volcano has allowed us to distinguish and quantify the crustal deformations of volcanic origin from deformations of different origin, which has always been a crucial question in the study of the crustal deformations of Mt. Etna.

[74] **Acknowledgments.** The authors wish to thank the Gruppo Analisi Dati Sismici (http://www.ct.ingv.it/ufs/analisti/catalogolist.php) of the Istituto Nazionale di Geofisica e Vulcanologia, Osservatorio Etneo for the elaboration of earthquakes data. Furthermore, we thank the Editor, André Revil, the Associate Editor, and the reviewers, M. Lisowski and P. Lundgren, for their comments and constructive suggestions that led to improve the original version of the manuscript.

## References

Aiuppa, A., et al. (2010), Patterns in the recent 2007–2008 activity of Mount Etna volcano investigated by integrated geophysical and geochemical observations, *Geochem. Geophys. Geosyst.*, *11*, Q09008, doi:10.1029/2010GC003168.

Allard, P., B. Behncke, S. D'Amico, M. Neri, and S. Gambino (2006), Mount Etna 1993–2005: Anatomy of an evolving eruptive cycle, *Earth Sci. Rev.*, *78*, 85–114, doi:10.1016/j.earscirev.2006.04.002.

Aloisi, M., O. Cocina, G. Neri, B. Orecchio, and E. Privitera (2002), Seismic tomography of the crust underneath the Etna volcano, Sicily, *Phys. Earth Planet. Inter.*, *134*, 139–155, doi:10.1016/S0031-9201(02)00153-X.

Aloisi, M., A. Bonaccorso, S. Gambino, M. Mattia, and G. Puglisi (2003), Etna 2002 eruption imaged from continuous tilt and GPS data, *Geophys. Res. Lett.*, *30*(23), 2214, doi:10.1029/2003GL018896.

Aloisi, M., A. Bonaccorso, F. Cannavò, S. Gambino, M. Mattia, G. Puglisi, and E. Boschi (2009), A new dyke intrusion style for the Mount Etna May 2008 eruption modelled through continuous tilt and GPS data, *Terra Nova*, *21*, 316–321, doi:10.1111/j.1365-3121.2009.00889.x.

Aloisi, M., M. Mattia, C. Ferlito, M. Palano, V. Bruno, and F. Cannavò (2011a), Imaging the multi-level magma reservoir at Mt. Etna volcano (Italy), *Geophys. Res. Lett.*, *38*, L16306, doi:10.1029/2011GL048488.

Aloisi, M., M. Mattia, C. Monaco, and F. Pulvirenti (2011b), Magma, faults, and gravitational loading at Mount Etna: The 2002–2003 eruptive period, *J. Geophys. Res.*, *116*, B05203, doi:10.1029/2010JB007909.

Altamimi, Z., X. Collilieux, J. Legrand, B. Garayt, and C. Boucher (2007), ITRF2005: A new release of the International Terrestrial Reference Frame based on time series of station positions and Earth Orientation Parameters, *J. Geophys. Res.*, *112*, B09401, doi:10.1029/2007JB004949.

Andronico, D., et al. (2005), A multi-disciplinary study of the 2002–2003 Etna eruption: Insights for a complex plumbing system, *Bull. Volcanol.*, *67*, 314–330, doi:10.1007/s00445-004-0372-8.

Andronico, D., A. Cristaldi, and S. Scollo (2008), The 4–5 September 2007 lava mountain at South-East Crater of Mt. Etna, Italy, *J. Volcanol. Geotherm. Res.*, *173*, 325–328, doi:10.1016/j.jvolgeores.2008.02.004.

Argnani, A., and C. Bonazzi (2005), Malta Escarpment fault zone offshore eastern Sicily: Pliocene-Quaternary tectonic evolution based on new multichannel seismic data, *Tectonics*, *24*, TC4009, doi:10.1029/2004TC001656.

Azzaro, R. (1997), Seismicity and active tectonics along the Pernicana Fault, Mt. Etna (Italy), *Acta Vulcanol.*, *9*, 7–14.

Azzaro, R. (1999), Earthquake surface faulting at Mount Etna volcano (Sicily) and implications for active tectonics, *J. Geodyn.*, *28*, 193–213, doi:10.1016/S0264-3707(98)00037-4.

Azzaro, R. (2004), Seismicity and active tectonics in the Etna Region: Constraints for a seismotectonic model, in *Mt. Etna: Volcano Laboratory*, *Geophys. Monogr. Ser.*, vol. 143, edited by A. Bonaccorso et al., pp. 205–220, AGU, Washington, D. C., doi:10.1029/143GM13.

Beavan, J., and J. Haines (2001), Contemporary horizontal velocity and strain rate fields of the Pacific-Australian plate boundary zone through New Zealand, *J. Geophys. Res.*, *106*, 741–770, doi:10.1029/2000JB900302.

Behncke, B., and M. Neri (2003), Cycles and trends in the recent eruptive behaviour of Mt. Etna (Italy), *Can. J. Earth Sci.*, *40*, 1405–1411, doi:10.1139/e03-052.

Behncke, B., S. Falsaperla, and E. Pecora (2009), Complex magma dynamics at Mount Etna revealed by seismic, thermal, and volcanological data, *J. Geophys. Res.*, *114*, B03211, doi:10.1029/2008JB005882.

Bianca, M., C. Monaco, L. Tortorici, and L. Cernobori (1999), Quaternary normal faulting in southeastern Sicily (Italy): A seismic source for the 1693 large earthquake, *Geophys. J. Int.*, *139*, 370–394, doi:10.1046/j.1365-246x.1999.00942.x.

Bonaccorso, A., and P. M. Davis (2004), Modeling of ground deformation associated with recent lateral eruptions: Mechanics of magma ascent and intermediate storage at Mt. Etna, in *Mt. Etna: Volcano Laboratory*, *Geophys. Monogr. Ser.*, vol. 143, edited by A. Bonaccorso et al., pp. 293–306, AGU, Washington, D. C., doi:10.1029/143GM18.

Bonaccorso, A., and D. Patanè (2001), Shear response to an intrusive episode at Mt. Etna volcano (January 1998) inferred through seismic and tilt data, *Tectonophysics*, *334*, 61–75, doi:10.1016/S0040-1951(01)00056-7.

Bonaccorso, A., S. D'Amico, M. Mattia, and D. Patanè (2004), Intrusive mechanisms at Mt. Etna forerunning the July August 2001 eruption, *Pure Appl. Geophys.*, *161*, 1469–1487, doi:10.1007/s00024-004-2515-4.

Bonaccorso, A., S. Cianetti, C. Giunchi, E. Trasatti, M. Bonafede, and E. Boschi (2005), Analytical and 3D numerical modeling of Mt. Etna (Italy) volcano inflation, *Geophys. J. Int.*, *163*(2), 852–862, doi:10.1111/j.1365-246X.2005.02777.x.

Bonaccorso, A., A. Bonforte, F. Guglielmino, M. Palano, and G. Puglisi (2006), Composite ground deformation pattern forerunning the 2004–2005 Mount Etna eruption, *J. Geophys. Res.*, *111*, B12207, doi:10.1029/2005JB004206.

Bonafede, M., M. Dragoni, and F. Quareni (1986), Displacement and stress fields produced by a centre of dilation and by a pressure source in a viscoelastic half-space: Application to the study of ground deformation and seismic activity at Campi Flegrei, Italy, *Geophys. J. R. Astron. Soc.*, *87*, 455–485, doi:10.1111/j.1365-246X.1986.tb06632.x.

Bonanno, A., M. Palano, E. Privitera, S. Gresta, and G. Puglisi (2011), Magma intrusion mechanisms and redistribution of seismogenic stress at Mt. Etna volcano (1997–1998), *Terra Nova*, *00*, 1–10, doi:10.1111/j.1365-3121.2011.01019.x.

Bonforte, A., and G. Puglisi (2003), Magma uprising and flank dynamics on Mount Etna volcano, studied using GPS data (1994–1995), *J. Geophys. Res.*, *108*(B3), 2153, doi:10.1029/2002JB001845.

Bonforte, A., A. Bonaccorso, G. Francesco, M. Palano, and G. Puglisi (2008), Feeding system and magma storage beneath Mt. Etna as revealed by recent inflation/deflation cycles, *J. Geophys. Res.*, *113*, B05406, doi:10.1029/2007JB005334.

Bonforte, A., F. Guglielmino, M. Coltelli, A. Ferretti, and G. Puglisi (2011), Structural assessment of Mount Etna volcano from Permanent Scatterers analysis, *Geochem. Geophys. Geosyst.*, *12*, Q02002, doi:10.1029/2010GC003213.

Borgia, A., L. Ferrari, and G. Pasquarè (1992), Importance of gravitational spreading in the tectonic and volcanic evolution of Mount Etna, *Nature*, *357*, 231–235, doi:10.1038/357231a0.

Borgia, A., R. Lanari, E. Sansosti, M. Tesauro, P. Berardino, G. Fornaro, M. Neri, and J. B. Murray (2000), Actively growing anticlines beneath Catania from distal motion of Mount Etna's decollement measured by SAR interferometry and GPS, *Geophys. Res. Lett.*, *27*, 3409–3412, doi:10.1029/1999GL008475.

Branca, S., and P. Del Carlo (2005), Types of eruptions of Etna volcano AD 1670–2003: Implications of short-term eruptive activity, *Bull. Volcanol.*, *67*, 732–742, doi:10.1007/s00445-005-0412-z.

Burollet, P. F., J. M. Muginot, and P. Sweeney (1978), The geology of the Pelagian Block: The margins and basins of southern Tunisia and Tripolitania, in *Ocean Basins and Margins*, edited by A. E. M. Nairn et al., pp. 331–359, Plenum, New York.

Burton, M. R., et al. (2005), Etna 2004–2005: An archetype for geodynamically-controlled effusive eruptions, *Geophys. Res. Lett.*, *32*, L09303, doi:10.1029/2005GL022527.

Corsaro, R. A., and M. Pompilio (2004), Dynamics of magmas at Mount Etna, in *Mt. Etna: Volcano Laboratory*, *Geophys. Monogr. Ser.*, vol. 143, edited by A. Bonaccorso et al., pp. 91–110, AGU, Washington, D. C., doi:10.1029/143GM07.

Davis, P. M. (1986), Surface deformation due to inflation of an arbitrarily oriented triaxial ellipsoidal cavity in an elastic half-space, with reference to Kilauea volcano, Hawaii, *J. Geophys. Res.*, *91*(B7), 7429–7438, doi:10.1029/JB091iB07p07429.

Dixon, T. H., M. M. Miller, F. Farina, H. Wang, and D. Johnson (2000), Present-day motion of Sierra Nevada block and some tectonic implications for the Basin and Range province: North America Cordillera, *Tectonics*, *19*, 1–24, doi:10.1029/1998TC001088.

Efron, B. (1982), *The Jackknife, the Bootstrap and Other Resampling Plans*, Soc. for Ind. and Appl. Math., Philadelphia, Pa., doi:10.1137/1.9781611970319.

Ferlito, C., and G. Lanzafame (2010), The role of supercritical fluids in the potassium enrichment of magmas at Mount Etna volcano (Italy), *Lithos*, *119*, 642–650, doi:10.1016/j.lithos.2010.08.006.

Ferlito, C., M. Coltorti, R. Cristofolini, and P. P. Giacomoni (2009), The contemporaneous emission of low-K and high-K trachybasalts and the role of the NE Rift during the 2002 eruptive event, Mt. Etna, Italy, *Bull. Volcanol.*, *71*, 575–587, doi:10.1007/s00445-008-0243-9.

Ferlito, C., M. Viccaro, E. Nicotra, and R. Cristofolini (2012), Regimes of magma recharge and their control on the eruptive behaviour during the period 2001–2005 at Mt. Etna volcano, *Bull. Volcanol.*, *74*, 533–543, doi:10.1007/s00445-011-0537-1.

Froger, J. L., O. Merle, and P. Briole (2001), Active spreading and regional extension at Mt. Etna imaged by SAR interferometry, *Earth Planet. Sci. Lett.*, *187*, 245–258, doi:10.1016/S0012-821X(01)00290-4.

Ellis, M., and G. C. P. King (1991), Structural control of flank volcanism in continental rifts, *Science*, *254*, 839–842, doi:10.1126/science.254.5033.839.

Gillot, P. Y., G. Kieffer, and R. Romano (1994), The evolution of Mount Etna in the light of potassium-argon dating, *Acta Vulcanol.*, *5*, 81–87.

Goldberg, D. E. (1989), *Genetic Algorithms in Search, Optimization and Machine Learning*, Addison-Wesley, Reading, Mass.

Groppelli, G., and A. Tibaldi (1999), Control of rock rheology on deformation style and slip-rate along the active Pernicana Fault, Mt. Etna, Italy, *Tectonophysics*, *305*, 521–537, doi:10.1016/S0040-1951(99)00035-9.

Guest, J. E., and J. B. Murray (1979), An analysis of hazard from Mount Etna volcano, *J. Geol. Soc. London*, *136*, 347–354, doi:10.1144/gsjgs.136.3.0347.

Gutenberg, B., and C. F. Richter (1956), Earthquake magnitude, intensity, energy and acceleration, *Bull. Seismol. Soc. Am.*, *46*, 105–145.

Haines, A. J., and W. E. Holt (1993), A procedure for obtaining the complete horizontal motions within zones of distributed deformation from the inversion of strain rate data, *J. Geophys. Res.*, *98*, 12,057–12,082, doi:10.1029/93JB00892.

Haines, A. J., A. Jackson, W. E. Holt, and D. C. Agnew (1998), Representing distributed deformation by continuous velocity fields, *Sci. Rep. 98/5*, Inst. of Geol. and Nucl. Sci., Lower Hutt, N. Z.

Herring, T. A. (2004), GLOBK: Global Kalman filter VLBI and GPS analysis program, version 10.2, user's manual, Mass. Inst. of Technol., Cambridge.

Hirn, A., A. Nercessian, M. Sapin, F. Ferrucci, and G. Wittlinger (1991), Seismic heterogeneity of Mt. Etna: Structure and activity, *Geophys. J. Int.*, *105*, 139–153, doi:10.1111/j.1365-246X.1991.tb03450.x.

Hirn, A., R. Nicolich, J. Gallart, M. Laigle, and L. Cernobori, and the ETNASEIS Scientific Group (1997), Roots of Etna volcano in faults of great earthquakes, *Earth Planet. Sci. Lett.*, *148*, 171–191, doi:10.1016/S0012-821X(97)00023-X.

Holt, W. E., and A. J. Haines (1995), The kinematics of northern South Islands, New Zealand, determined from geologic strain rates, *J. Geophys. Res.*, *100*, 17,991–18,010, doi:10.1029/95JB01059.

Imbò, G. (1928), Sistemi eruttivi etnei [in Italian], *Bull. Volcanol, Ser. I*, *5*, 89–119.

King, R. W., and Y. Bock (2004), Documentation of the MIT GPS Analysis Software: GAMIT, release 10.2, user's manual, Mass. Inst. of Technol., Cambridge.

Kreemer, C., W. E. Holt, S. Goes, and R. Govers (2000), Active deformation in eastern Indonesia and the Philippines from GPS and seismicity data, *J. Geophys. Res.*, *105*(B1), 663–680, doi:10.1029/1999JB900356.

Lahr, J. C. (1989), Hypoellipse version 2.0: A computer program for determining local earthquake hypocentral parameters, magnitude and first motion pattern, *U.S. Geol. Surv. Open File Rep.*, *89/116*, 81 pp.

Lewis, R. M., and V. Torczon (1999), Pattern search algorithms for bound constrained minimization, *SIAM J. Optim.*, *9*(4), 1082–1099, doi:10.1137/S1052623496300507.

Lo Giudice, E., G. Patanè, R. Rasà, and R. Romano (1982), The structural frame work of Mount Etna, *Mem. Soc. Geol. Ital.*, *23*, 125–158.

Lundgren, P., F. Casu, M. Manzo, A. Pepe, P. Berardino, E. Sansosti, and R. Lanari (2004), Gravity and magma induced spreading of Mount Etna volcano revealed by satellite radar interferometry, *Geophys. Res. Lett.*, *31*, L04602, doi:10.1029/2003GL018736.

Maaz, R., W. Ullmann, and V. Kbrnik (1974), Map of the seismic energy flux: Example of western Greece, *Pure Appl. Geophys.*, *112*, 5–9, doi:10.1007/BF00875911.

Makris, J., R. Nicolich, and W. Weigel (1986), A seismic study in the western Ionian sea, *Ann. Geophys.*, *6B*, 665–678.

Mao, A., C. G. A. Harrison, and T. H. Dixon (1999), Noise in GPS coordinate time series, *J. Geophys. Res.*, *104*(B2), 2797–2816, doi:10.1029/1998JB900033.

Mastin, L. G., E. Roeloffs, N. M. Beeler, and J. E. Quick (2008), Constraints on the size, overpressure, and volatile content of the Mount St. Helens Magma system from geodetic and dome growth measurements during the 2004–2006+ Eruption, in *A Volcano Rekindled: The Renewed Eruption of Mount St. Helens*, edited by D. R. Sherrod, W. E. Scott, and P. H. Stauffer, *U.S. Geol. Surv. Prof. Pap.*, 1750, pp. 461–488.

Mastin, L. G., M. Lisowski, E. Roeloffs, and N. Beeler (2009), Improved constraints on the estimated size and volatile content of the Mount St. Helens magma system from the 2004–2008 history of dome growth and deformation, *Geophys. Res. Lett.*, *36*, L20304, doi:10.1029/2009GL039863.

Mattia, M., M. Palano, V. Bruno, and F. Cannavò (2009), Crustal motion along the Calabro-Peloritano Arc as imaged by twelve years of measurements on a dense GPS network, *Tectonophysics*, *476*, 528–537, doi:10.1016/j.tecto.2009.06.006.

Mattia, M., V. Bruno, F. Cannavò, and M. Palano (2011), Evidences of a contractional pattern along the northern rim of the Hyblean Plateau (Sicily, Italy) from GPS data, *Geol. Acta*, *10*, 63–70.

McCaffrey, R., A. I. Qamar, R. W. King, R. Wells, G. Khazaradze, C. A. Williams, C. W. Stevens, J. J. Vollick, and P. C. Zwick (2007), Fault locking, block rotation and crustal deformation in the Pacific Northwest, *Geophys. J. Int.*, *169*, 1315–1340, doi:10.1111/j.1365-246X.2007.03371.x.

McGuire, W. J., and A. D. Pullen (1989), Location and orientation of eruptive fissures and feeder-dykes at Mount Etna: Influence of gravitational and regional tectonic stress regimes, *J. Volcanol. Geotherm. Res.*, *38*, 325–344, doi:10.1016/0377-0273(89)90046-2.

McGuire, W. J., J. L. Moss, S. J. Saunders, and I. S. Stewart (1996), Dike-induced rifting and edifice instability at Mount Etna, paper presented at Etna: Fifteen Years On, Cheltenham and Gloucester Coll. of Higher Educ., Gloucestershire, U. K.

McTigue, D. F. (1987), Elastic stress and deformation near a finite spherical magma body: Resolution of the point source paradox, *J. Geophys. Res.*, *92*, 12,931–12,940, doi:10.1029/JB092iB12p12931.

Mogi, K. (1958), Relations between the eruptions of various volcanoes and the deformations of the ground surface around them, *Bull. Earthquake Res. Inst.*, *36*, 99–134.

Monaco, C., L. Petronio, and M. Romanelli (1995), Tettonica estensionale nel settore orientale del Monte Etna (Sicilia): Dati morfotettonici e sismici, [in Italian], *Stud. Geol. Camerti*, *2*, 363–374.

Monaco, C., P. Tappoiner, L. Tortorici, and P. Y. Gillot (1997), Late Quaternary slip rates on the Acireale-Piedimonte normal faults and tectonic origin of Mt. Etna (Sicily), *Earth Planet. Sci. Lett.*, *147*, 125–139, doi:10.1016/S0012-821X(97)00005-8.

Monaco, C., S. Catalano, O. Cocina, G. De Guidi, C. Ferlito, S. Gresta, C. Musumeci, and L. Tortorici (2005), Tectonic control on the eruptive dynamics at Mt. Etna Volcano (Sicily) during the 2001 and 2002–2003 eruptions, *J. Volcanol. Geotherm. Res.*, *144*, 211–233, doi:10.1016/j.jvolgeores.2004.11.024.

Monaco, C., G. De Guidi, and C. Ferlito (2010), The morphotectonic map of Mt. Etna, *Ital. J. Geosci.*, *129*(3), 408–428.

Murru, M., C. Montuori, M. Wyss, and E. Privitera (1999), The locations of magma chambers at Mt. Etna, Italy, mapped by *b*-values, *Geophys. Res. Lett.*, *26*(16), 2553–2556, doi:10.1029/1999GL900568.

Neri, M., and V. Acocella (2006a), The 2004–2005 Etna eruption: Implications for flank deformation and structural behaviour of the volcano, *J. Volcanol. Geotherm. Res.*, *158*, 195–206, doi:10.1016/j.jvolgeores.2006.04.022.

Neri, M., V. Acocella, and B. Behncke (2004), The role of the Pernicana Fault System in the spreading of Mount Etna (Italy) during the 2002–2003 eruption, *Bull. Volcanol.*, *66*, 417–430, doi:10.1007/s00445-003-0322-x.

Neri, M., B. Behncke, M. Burton, G. Galli, S. Giammanco, E. Pecora, E. Privitera, and D. Reitano (2006b), Continuous soil radon monitoring during the July 2006 Etna eruption, *Geophys. Res. Lett.*, *33*, L24316, doi:10.1029/2006GL028394.

Nicolich, R., M. Laigle, A. Hirn, L. Cernobori, and J. Gallart (2000), Crustal structure of the Ionian margin of Sicily: Etna volcano in the frame of regional evolution, *Tectonophysics*, *329*, 121–139, doi:10.1016/S0040-1951(00)00192-X.

Palano, M., G. Puglisi, and S. Gresta (2008), Ground deformation patterns at Mt. Etna from 1993 to 2000 from joint use of InSAR and GPS techniques, *J. Volcanol. Geotherm. Res.*, *169*, 99–120, doi:10.1016/j.jvolgeores.2007.08.014.

Palano, M., S. Gresta, and G. Puglisi (2009), Time-dependent deformation of the eastern flank of Mt. Etna: After-slip or viscoelationastic relaxation?, *Tectonophysics*, *473*, 300–311, doi:10.1016/j.tecto.2009.02.047.

Palano, M., M. Rossi, F. Cannavò, V. Bruno, M. Aloisi, D. Pellegrino, M. Pulvirenti, G. Siligato, and M. Mattia (2010), Etn@ref: A geodetic reference frame for Mt. Etna GPS networks, *Ann. Geophys.*, *53*(4), 49–57.

Patanè, D., and E. Privitera (2001), Seismicity related to 1989 and 1991–93 Mt. Etna (Italy) eruptions: Kinematic constraints by FPS analysis, *J. Volcanol. Geotherm. Res.*, *109*, 77–98, doi:10.1016/S0377-0273(00)00305-X.

Patanè, D., M. Mattia, and M. Aloisi (2005), Shallow intrusive processes during 2002–2004 and current volcanic activity on Mt. Etna, *Geophys. Res. Lett.*, *32*, L06302, doi:10.1029/2004GL021773.

Puglisi, G., P. Briole, and A. Bonforte (2004), Twelve years of ground deformation studies on Mt. Etna volcano based on GPS surveys, in *Mt. Etna: Volcano Laboratory*, *Geophys. Monogr. Ser.*, vol. 143, edited by A. Bonaccorso et al., pp. 321–341, AGU, Washington, D. C., doi:10.1029/143GM20

Puglisi, G., A. Bonforte, A. Ferretti, F. Guglielmino, M. Palano, and C. Prati (2008), Dynamics of Mount Etna before, during, and after the July–August 2001 eruption inferred from GPS and differential synthetic aperture radar interferometry data, *J. Geophys. Res.*, *113*, B06405, doi:10.1029/2006JB004811.

Rasà, R., R. Azzaro, and O. Leonardi (1996), Aseismic creep on faults and flank instability at Mt. Etna volcano, *Geol. Soc. Spec. Publ.*, *110*, 179–192, doi:10.1144/GSL.SP.1996.110.01.14.

Rust, D., B. Behncke, M. Neri, and A. Ciocanel (2005), Nested zones of instability in the Mount Etna volcani edifice, Italy, *J. Volcanol. Geotherm. Res.*, *144*, 137–153, doi:10.1016/j.jvolgeores.2004.11.021.

Solaro, G., V. Acocella, S. Pepe, J. Ruch, M. Neri, and E. Sansosti (2010), Anatomy of an unstable volcano from InSAR: Multiple processes affecting flank instability at Mt. Etna, 1994–2008, *J. Geophys. Res.*, *115*, B10405, doi:10.1029/2009JB000820.

Tiampo, K. F., J. B. Rundle, J. Fernandez, and J. O. Langbein (2000), Spherical and ellipsoidal volcanic sources at Long Valley caldera, California, using a genetic algorithm inversion technique, *J. Volcanol. Geotherm. Res.*, *102*, 189–206, doi:10.1016/S0377-0273(00)00185-2.

Wadge, G., G. P. L. Walker, and J. E. Guest (1975), The output of the Etna volcano, *Nature*, *213*, 484–485.

Williams, C. A., and G. Wadge (1998), The effects of topography on magma chamber deformation models: Application to Mt. Etna and radar interferometry, *Geophys. Res. Lett.*, *25*(10), 1549–1552, doi:10.1029/98GL01136.

Williams, C. A., and G. Wadge (2000), An accurate and efficient method for including the effects of topography in three-dimensional elastic models of ground deformation with applications to radar interferometry, *J. Geophys. Res.*, *105*(B4), 8103–8120, doi:10.1029/1999JB900307.

Yang, X. M., P. M. Davis, and J. H. Dieterich (1988), Deformation from inflation of a dipping finite prolate spheroid in an elastic half-space as a model for volcanic stressing, *J. Geophys. Res.*, *93*, 4249–4257, doi:10.1029/JB093iB05p04249.